Article:

Xu, H., Li, Z., Dong, H. et al. (2017) Hemodynamic parameters that may predict false-lumen growth in type-B aortic dissection after endovascular repair: A preliminary study on long-term multiple follow-ups. Medical Engineering & Physics, 50. pp. 12-21. ISSN: 1350-4533

https://doi.org/10.1016/j.medengphy.2017.08.011

Hemodynamic Parameters That May Predict False-lumen Growth in Type-B Aortic Dissection after Endovascular Repair: A Preliminary Study on Long-term Multiple Follow-ups

Huanming Xu[1,2], Zhenfeng Li[1,2], Huiwu Dong[3], Yilun Zhang[1], Jianyong Wei[1], Paul N. Watton[5,6], Wei Guo[7], Duanduan Chen[1,2]*, Jiang Xiong[7]*

[1]School of Life Science, Beijing Institute of Technology, China
[2]Key Laboratory of Convergence Medical Engineering System and Healthcare Technology, The Ministry of Industry and Information Technology, Beijing Institute of Technology, China
[3]Department of Ultrasound Diagnosis, Chinese PLA General Hospital, China
[5]Department of Computer Science & INSIGNEO Institute, University of Sheffield, UK
[6]Department of Mechanical Engineering and Material Science, University of Pittsburgh
[7]Department of Vascular and Endovascular Surgery, Chinese PLA General Hospital, China

***Corresponding author:** Prof Duanduan Chen
School of Life Science, Beijing Institute of Technology, Beijing,
100081, China.
Tel. +86-10-68912154
Email. duanduan@bit.edu.cn

Dr Jiang Xiong
Department of Vascular and Endovascular Surgery,
Chinese PLA General Hospital, Beijing, 100853, China.
Tel. +86-10-66938349
Email. xiongjiangdoc@126.com

ABSTRACT

Thoracic endovascular aortic repair (TEVAR) is commonly applied in type-B aortic dissection. For patients with dissection affects descending aorta and extends downward to involve abdominal aorta and possibly iliac arteries, false lumen (FL) expansion might occur post-TEVAR. Predictions of dissection development may assist in medical decision on re-intervention or surgery. In this study, two patients are selected with similar morphological features at initial presentation but with different long-term FL development post-TEVAR (stable and enlarged FL). Patient-specific models are established for each of the follow-ups. Flow boundaries and computational validations are obtained from Doppler ultrasound velocimetry. By analyzing the hemodynamic parameters, the false-to-true luminal pressure difference (PDiff) and particle relative residence time (RRT) are found related to FL remodeling. It is found that (i) the position of the first FL flow entry is the watershed of negative-and-positive PDiff and, in long-term follow-ups, and the position of largest PDiff is consistent with that of the greatest increase of FL width; (ii) high RRT occurs at the FL proximal tip and similar magnitude of RRT is found in both stable and enlarged cases; (iii) comparing to the RRT at 7days post-TEVAR, an increase of RRT afterwards in short-term is found in the stable case while a slight decrease of this parameter is found in the enlarged case, indicating that the variation of RRT in short-term post-TEVAR might be potential to predict long-term FL remodeling.

Key Words: aortic dissection; hemodynamics; endovascular procedures.

INTRODUCTION

Aortic dissection (AoD) is a severe cardiovascular disease, where a surge of blood flowing into the aortic wall via an initial tear or damage of the intima and splitting the single aortic lumen into a true and false lumen (TL and FL). Stanford type-B AoD indicates those with the dissection begins distal to the supraaortic branches. Interventional treatment of Stanford type-B AoD commonly involves thoracic endovascular aortic repair (TEVAR)[1]. In a number of patients, FL expansion is found post-TEVAR, especially in the infrarenal aorta. Recent study confirmed that abdominal aortic expansion can be frequently found after TEVAR and is independent from thoracic FL thrombosis[2]. Prediction of FL growth may contribute to early decision-making of re-intervention or surgery. The post-TEVAR development of dissection is highly dependent on local hemodynamics[3]. Medical imaging tools such as Doppler ultrasound[4] and phase-contrast MR (pcMR)[5] are able to capture the flow velocity within aorta. However, the former provides velocity information at a certain position of the vessel, and the latter reveals flow movement with relatively low spatial and temporal resolution[6, 7]. On the other hand, the uptake of ^{18}F-fluorodeoxyglucose in PET-CT can indicate complications in AoD[8] and positive correlation between the uptake and wall shear stress is found in aortic aneurysm study[9]; however, PET-CT is relatively expensive and the flow information cannot be directly reported. Thus, computational simulations that can provide hemodynamic parameters, such as flow, pressure and shear stress distributions, may enrich analysis.

Previous computational works focusing on type-B AoD include investigations on hemodynamic features[10-14], luminal flow exchange[12, 15], post-TEVAR flow effects[16-18], tear-induced flow effects[19, 20] and fluid-structure interaction studies[21, 22]. Besides, 4D pcMR[5, 23] and phantom[24, 25] measurements have been conducted to compare with or validate the computed results. In this study, we investigate the flow-driven dissection development after TEVAR based on long-term multiple follow-ups. Flow conditions in patients with stable and enlarged FL are compared and key hemodynamic parameters that are related to dissection growth in abdominal aorta are proposed, facilitating medical decision-making on post-TEVAR treatment.

METHODS

Image Acquisition and Model Reconstruction

This study was approved by the institutional review board of the Chinese PLA General Hospital. Written informed consent was obtained from the patients involved in this study. Two male patients (PI and PII) with subacute Stanford type-B AoD underwent arterial-phase CT angiography (CTA) at initial presentation and during the follow-up examinations after TEVAR via a dual-source CT scanner (SOMATOM Definition Flash, SIEMENS, Germany). Details of the CTA scan and the patient information are described in S1, Supporting Document. Image segmentation and surface reconstruction of AoD were conducted through Mimics (Materialise, Belgium). The cross-sectional contours of the reconstructed geometries were mapped back to CTA images to ensure that the 3D models present the actual outline of the vessel lumen. Detailed views of the models are shown in Fig.1, where PI/II-1 indicates the models pre-TEVAR while PI/II-2 and others are models post-TEVAR. After TEVAR, PI and PII have experienced six- (7days~53months) and four-times (7days~35months) CTA scans. The FL in PI was in stable condition (PI-2~7, Fig.1b) while that in PII was expanding (PII-2~5, Fig.1d). The models were meshed in ICEM (ANSYS Inc, Canonsburg, USA) with tetrahedral elements in the core region and prismatic cells (10 layers) in the boundary layer near the aortic wall. The grid resolution varies from 2,564,019 to 3,153,829 cells.

Doppler Ultrasound and Boundary Conditions

Time-variant velocities at ascending aorta (AAo), brachiocephalic trunk (BT), left common carotid artery (LCCA), left subclavian artery (LSA) were measured via Doppler ultrasound of the patients, and velocity variation at the distal thoracic aorta (DTAo, about 5cm above celiac trunk) was measured in the final examination of PI to provide validation of the computational results. This is because the true lumen (TL) remodeling at this position in PI is sufficient, so that relatively organized flow is found and the central line of vessel can be accurately identified. The velocity of AAo was measured through the apical 5-chamber view and the suprasternal long axis view of aortic arch. The two results were compared to ensure the maximum velocity at AAo could be captured. For other arteries (BT, LCCA, LSA and DTAo), Doppler velocimetry has been conducted at the proximal and distal sites of the targeted measurement vessel. Mean velocity over a cardiac cycle at the two sites for each particular vessel was then calculated and compared. When the difference between them is less than 5%, the measured velocity is considered effective. Details of the measurement are described in S2, Supporting Document.

The upper edge of the velocity sonogram was extracted (Fig.1e) as the variation of the maximum velocity at the measured site. The flow rates at AAo, BT, LCCA and LSA, as the velocity boundary conditions, can then be calculated based on the measured time-variant maximum velocity and the assumed flat flow profile for AAo and parabolic flow profile for the others. The velocity boundary conditions of the models is shown in Fig.S1a, Supporting Document. Pulsatile waveforms of the pressure at celiac artery (CA), superiormesenteric artery (SMA), renal arteries and the outlets at common iliac arteries were obtained from previous study[26] (Fig.S1b, Supporting Document). As shown in Fig.1, two models in PII (PII-1 and PII-4) were cropped below the iliac bifurcation due to the relatively shorter CT scanning range. To eliminate the outlet effects, time-variant pressure distribution at the cropping plane has been calculated in PII-2~3 and PII-5. The averaged pressure information at this cropping plane was mapped to PII-1 and PII-4, serving as the pulsatile pressure outlets.

Numerical Models

The vessel wall was assumed as no-slip and rigid, due to low distensibility in long-term follow-ups[27]. The blood was treated as Newtonian and incompressible with density of 1044kg/m^3 and dynamic viscosity of 0.00365kg·m^{-1}·s^{-1}[28]. The average Reynolds number over a cardiac cycle, calculated based on the equivalent diameter ($D_e = 2\sqrt{Area/\pi}$) and velocity at the inlet of the ascending aorta in PI and PII, were between 2066-2197 and 2844-2960, respectively. Our previous study confirmed that laminar simulations with adequately fine mesh resolutions, especially refined near the walls, can capture flow patterns as turbulence model[15]. To further confirm this, we solved the flow in the first follow-up cases (PI-2 and PII-2) by both laminar and k-ω SST turbulence models, where the flow in the abdominal aortic region is the fastest during the follow-ups. Similar flow patterns were found and the discrepancy of the maximum velocity and wall shear stress (WSS) in the abdominal aorta was 4.2% and 5.2% respectively (the laminar and turbulent results of PII-2 were shown in Fig.S2, Supporting Document), ensuring the rationality of laminar model to be applied in the current problem. A finite volume solver, CFD-ACE+ (ESI Group, France) was employed. The heart-beat cycle of the patients was measured at each clinical examination. The averaged cardiac cycle for PI and PII were 71 and 69beat/min respectively. Temporal discretization of numerical models was assigned as 45step/cycle. Simulation was carried out for 5 cardiac cycles to achieve a periodic solution and results of the final cycle were presented. Grid and temporal independency analyses on finer grids and finer temporal discretizations were conducted to ensure the base resolution with the base time step settings are adequate (S3, Supporting Document).

RESULTS

Aortic Remodeling

Aortic remodeling was assessed by: (i) size and numbers of the aortic tears (AoT), (ii) change of luminal volume, and (iii) growth of aortic diameter. There are four major AoTs along the aorta for both patients at initial presentation. The primary entry (AoT-1) in both patients is located at the proximal region of descending aorta and the locations of other AoTs (AoT-2~4) are displayed in Fig.1. After TEVAR, the primary entry was sealed and after the first follow-up of PI, AoT-2 was disappeared. Considering the position and local aortic curvature of the tears, AoT-4 is the exit of the flow from FL to TL, while the function of AoT-2 and AoT-3 is uncertain. Since only the flow entries towards the FL is able to bring mechanical impact into the dissection, size measurement was only performed on AoT-2 and AoT-3 (Table 1). Post-TEVAR, both AoT-2 and AoT-3 in PI and PII are enlarged, probably due to the greater flow impact on these sites after AoT-1 was sealed.

Table 1. The size of the aortic tears in the patients with long-term follow-ups

Tear	Geometry	PI-1	PI-2	PI-3	PI-4	PI-5	PI-6	PI-7
AoT-2	H[mm]	7.87	7.15	-	-	-	-	-
	W[mm]	8.97	10.76	-	-	-	-	-
	A[mm^2]	64.61	70.71	-	-	-	-	-
AoT-3	H[mm]	13.86	18.79	17.93	15.31	18.23	8.81	8.57
	W[mm]	10.04	9.38	6.03	8.90	7.30	6.72	5.75
	A[mm^2]	116.13	150.82	106.40	119.19	128.82	93.49	44.09
Tear	Geometry	PII-1	PII-2	PII-3	PII-4	PII-5		
AoT-2	H[mm]	8.17	8.41	5.74	11.04	11.20		
	W[mm]	9.34	9.96	7.36	9.59	6.03		
	A[mm^2]	62.61	70.47	37.33	89.50	54.05		
AoT-3	H[mm]	9.91	9.55	7.77	6.25	6.19		
	W[mm]	10.01	11.47	9.34	8.04	9.90		
	A[mm^2]	85.27	99.32	61.51	40.35	53.32		

H-Height; W-Width; A-Area.

The change of luminal volume is shown in Fig.2. The volume of TL (V_{TL}) involves the initial dissection-affected TL region, while $V_{TL\text{-}Part}$ indicates the dissection-affected TL region during the follow-ups. Variations of V_{TL}, volume of FL (V_{FL}) and the ratio between $V_{TL\text{-}Part}$ and V_{FL} are displayed in Fig.2b. V_{FL} in the stable case (PI) reduces gradually post-TEVAR, except for the final examination, where a trivial increase of V_{FL} is found (131.6mm^3 in 20months). However, V_{FL} in the expanding case (PII) reduces in the first two follow-ups but enlarges afterwards, where the V_{FL} growths in PII-4 and PII-5 are 2,138mm^3 and 34,989mm^3 respectively, the durations of which are both 17months (Fig.2b). For both cases, the TL-to-FL volume ratio ($V_{TL\text{-}Part}/V_{FL}$) keeps increasing, except for PI-6 and PII-3 (pointed by arrows). This is because significant FL regression occurs at the proximal region (blue squares in Fig.1b,1d), which shortens the comparison region. Since TL remodeling is insufficient in this region, value of $V_{TL\text{-}Part}/V_{FL}$ reduces. The averaged increase rates of $V_{TL\text{-}Part}/V_{FL}$ in the follow-ups of PI and PII are 1.8% and 0.3% per month, respectively, indicating a significant luminal remodeling difference.

The aortic diameter (D) is measured in each model, taking into account the width of TL and FL (W_{TL} and W_{FL}) and the thickness of flap. As shown in Fig.1f, measurements have been conducted in the axial plane of the CTA datasets, along a line that crosses the centre of the flap and is perpendicular to the flap. Four measurement positions are selected in the abdominal aorta. As shown in Fig.2a, they are 1cm below diaphragm (L1), 1cm above CA (L2), 3.5cm below SMA (L3) and 9cm below SMA (L4). Fig.2c~e display the variation of D, W_{TL} and W_{FL} respectively. Positive TL remodeling is found in PI and PII in general, except for L3 and L4 in PI-3 and L3 in PII-4~5. W_{FL} at the proximal region of PI (L1 and L2) reduces greatly during the follow-up, while in the distal region (L3 and L4), variation of W_{FL} is stable. In PII, W_{FL} increases sharply since the second follow-up (PII-3). Comparing the variation of W_{TL}, W_{FL} and D, it can be found that the variation pattern of D is mainly determined by the variation of W_{FL}.

Flow Pattern, Validation and Luminal Flow Exchange

Fig.3 shows the flow streamlines at systolic peak where the color map of velocity magnitude is restricted to a certain range in PI (0~2.51m/s) and PII (0~3.78m/s) to assist visualization of the longitudinal velocity variation. At systolic peak, fast and organized flow is found in TL; while vortical and relatively slow flow presents in FL. Highest velocity presents in the short-term follow-ups (PI-2~3, 4months for PI; PII-2~3, 1months for PII) at the region below stentgraft and above AoT-2 and -3, where TL remodeling is insufficient and the blood has not been diverted. In long-term follow-ups (PI-4~7 and PII-4~5), the flow in the proximal FL is generally slow (<0.5mm/s); while below AoT-2 (the first re-entry), where blood perfusion occurs, faster flow up to 1.53m/s in PI and 2.22m/s in PII are found in the FL with helical feature (Fig.3c).

To validate the computational results, Doppler ultrasound velocimetry was performed at distal thoracic aorta (5cm above CA) along the centerline of TL. This was only conducted at the final examination of PI, because its TL in the distal thoracic aorta is fully remodeled and the local flow is therefore organized (Fig.3a). The measured and computed velocities at the centre of the cross-section of the vessel, 5cm above CA, are 1.58m/s and 1.66m/s respectively, indicating a difference of 5.1%. Moreover, the computed velocity variation pattern is similar to the measured one (Fig.S3, Supporting Document), ensuring the rationality of computational results.

Fig.4 displays the luminal flow exchange via the primary entry for initial presentation and that via AoT-2 and AoT-3 during the follow-ups. As abovementioned, AoT-4 functions as the outlet of FL throughout the cardiac cycle, thus it is not displayed in Fig.4. As shown in Fig.4a (positive values indicates flow enters FL), before treatment, the TL-to-FL flow exchange in PI and PII presents similar pattern: the primary entry serves as the main flow inlet of FL; AoT-2 functions as the outlet of FL in the initial part of systole and behaves as inlet in the rest part of cardiac cycle; and AoT-3 mainly serves as the outlet of FL. There are 31.48% and 40.00% of the total flow diverted to FL over a cardiac cycle for PI and PII respectively, at initial presentation. After TEVAR, the function of the tears changes. In PI, AoT-2 becomes the inlet of FL in the entire heart-beat cycle (Fig.4b), while AoT-3 functions as the inlet of FL during systole and serves as the outlet in diastole (Fig.4c). Since the second follow-up of PI, AoT-2 is closed and AoT-3 gradually becomes the inlet of FL throughout the entire cardiac cycle. The flow entering FL are 16.67%, 6.98%, 8.24%, 9.59%, 5.43%, 3.09% of the total flow for case PI-2~7 respectively, the variation of which is consistent to the variation of tear size (Table 1) and it is generally reducing. In PII, both of AoT-2 and AoT-3 are existed during the follow-ups. AoT-2 mainly serves as the inlet of FL; especially in model PII-4 and PII-5, positive values of mass flow rate are found in the entire cardiac cycle (Fig.4b). AoT-3 diverts a small amount of flow into the FL during systole and mainly behaves as the outlet of FL (Fig.4c). There are 5.22%, 3.06%, 14.76% and 10.23% of the total flow diverted into FL in case PII-2~5 respectively, the variation of which is also consistent with the variation of tear size.

Loading Distribution along the Aorta

Fig.5a~b display the pressure drop at systolic peak (PDsys, the difference between the local pressure and the pressure at the bottom of the model). In TL, PDsys reduces from the inlet of AAo to the outlets of common iliac arteries. At initial presentation (PI-1 and PII-1), FL diverts part of the total flow (31.48% for PI and 40.00% for PII), maintaining PDsys in relatively low values. After TEVAR, in short-term follow-ups (PI-2~3 and PII-2~3), proximal descending aorta is supported by stentgraft and reshaped; however, below the endograft, TL remains collapsed, inducing larger resistance and resulting in higher velocity and regional lower pressure in this region (indicated by arrows in Fig.5a~b). In long-term follow-ups (PI-4~7 and PII-4~5), TL remodeling in distal thoracic aorta is improved; PDsys thus gradually reduces along aorta. In contrary, PDsys in FL is relatively uniform, which is probably due to the higher energy exchange induced by the vortical flow. Fig.5d shows the variation of the maximum PDsys during the follow-ups. For both patients, the maximum PDsys increases greatly soon after TEVAR (7days); along with the progress of TL remodeling, the maximum PDsys reduces. The PDsys in normal aorta model (Fig.5c) based on the same boundary conditions as PI and PII is also computed and the averaged maximum PDsys is shown by the dash line in Fig.5d. Since the growth of FL in the two patients shows obvious difference, the similar variation pattern of PDsys indicates that the pressure drop is mainly affected by TL remodeling.

The mean arterial pressure drop (PDmean) from AAo to the common iliac arteries during a cardiac cycle is also calculated. It is 6.29mmHg for the initial model of PI and 4.70mmHg for the final model (53months post-TEVAR), which is slightly higher than that in normal aorta for the studied segment (4mmHg[29]). The PDmean of PII at the initial and final (35months post-TEVAR) models are 6.53mmHg and 6.07mmHg, respectively, consistent with its insufficient TL remodeling.

In the final examination of PI (PI-7), V_{FL} is slightly increased, D and W_{FL} also increase at L3 (Fig.2); however, the flow exchange and tear size at this stage are both reduced. Fig.5e displays the pressure distribution at systolic peak (Psys) on a slice of FL for PI-6~7. It shows that the smaller tear size reduces the flow entering FL, however, it increases the velocity and induces higher pressure impact on the outer wall of FL (indicated by arrows in Fig.5e). The highest pressure of the impact region in PI and PII at final examination are 114.37 and 115.41mmHg respectively. Besides, by blanking the region with Psys<109.15mmHg, which is the 95% of the averaged maximum pressure in PI and PII at final examination, Fig.5f shows that the high pressure region (in red) in the FL of PII is much larger than that in PI. In fact, the FL growth rates of PI and PII at the final examination are $0.22mm^3$/day and $68.61mm^3$/day respectively.

Luminal Pressure Difference, Wall Shear Stress and Relative Residence Time

To investigate the pressure difference (PDiff) between TL and FL, a series of slices that are perpendicular to the centerline of TL are extracted and the net pressures in TL (P_{TL}) and FL (P_{FL}) on each slice over a cardiac cycle are calculated. Fig.6 displays PDiff (PDiff=P_{FL}-P_{TL}) in each model. In both patients, pre-TEVAR (Fig.6a,6e), P_{FL} is smaller than P_{TL} at the level above AoT-2; while, below AoT-2, P_{FL} is larger than P_{TL}, pushing the FL towards TL. Post- TEVAR, the primary entry is closed. In PI, negative values of PDiff are found above AoT-3 (Fig.6b~c), indicating higher P_{TL} presents in this region, which supports the aortic wall and assists in TL expansion. However, in the region below AoT-3 in PI, due to the blood perfusion into the FL, positive values of PDiff present, indicating FL propulsion on the TL. In the final follow-up of PI (Fig.6d), the maximum value of PDiff is 0.22mmHg. This maximum PDiff occurs close to L3. At this position, W_{FL} and W_{TL} increase by 1.02mm and 0.46mm respectively (Fig.2), indicating this small value of PDiff (0.22mmHg) is not large enough to squeeze TL but the local pressure in FL (Fig.5e) is able to induce further FL expansion. On the other hand, in PII, post-TEVAR, AoT-2 becomes the main inlet of the flow into FL. Higher above this tear, P_{TL} is larger than P_{FL}, supporting TL expansion (Fig.6e~f). In the near region above AoT-2, TL remodeling is insufficient for the short-term follow-ups but P_{FL} gradually increases; thus, regional positive PDiff is found in PII-3 above AoT-2 (arrow indicated in Fig.6f). Below AoT-2, positive values of PDiff dominate and the maximum PDiff in the final examination of PII is 1.39mmHg, more than 6-times as high as that in PI, occurring close to L3. Taking account of that, in PII-5, W_{TL} decreases yet W_{FL} increases at L3 (Fig.2d~e), this high PDiff propels TL collapse and the local pressure pushes FL growth.

Fig.7 shows the wall shear stress (WSS) distribution on the flap at systolic peak. Its variation over a cardiac cycle is shown in Video S1-6, Supporting Document. In both patients, the WSS on the flap at the FL side (WSS_{FL}) is significantly smaller than that on the TL side (WSS_{TL}); and the WSS_{TL} in PII is generally higher than that in PI. At initial presentation, the maximum WSS_{TL} occurs at the edge of primary entry; while the maximum WSS_{FL} occurs at the proximal descending aorta along the side opposite to the primary entry (indicated by arrows in Fig.7b). In follow-ups, the maximum WSS_{TL} occurs at the region where TL presents most collapse; while the maximum WSS_{FL} occurs at the edge of the tears. AoT-3 and AoT-2 are the main FL flow entries for PI and PII in follow-ups, which induces helical flow in the downstream and high WSS_{FL} on the side opposite to the tears (indicated by hollow arrows in Fig.7b). To further visualize the variation of WSS_{FL} at different regions along the flap on the FL side, the color map is assigned to 0~5Pa (Fig.7c) and 0~0.5Pa (Fig.7d) to show the distal and proximal region respectively. In PI, WSS_{FL} at the region below AoT-3 reduces obviously from PI-4 to PI-6; however, in the final examination, it is slightly increased, although the maximum WSS_{FL} in this region is still smaller than 1Pa. In PII, WSS_{FL} presents obvious increase in PII-4 and reduces slightly in PII-5; the maximum WSS_{FL} at the region between AoT-2 and AoT-3 in the final examination is 5.21Pa.

Particle residence time is proposed to be related to thrombosis establishment[14].

The relative residence time (RRT), which is based on the time-averaged WSS (TAWSS) and oscillatory shear index (OSI), $[(1-2\cdot OSI)\cdot TAWSS]^{-1}$, reflects particle residence time and thus may correspond with the region of thrombosis[14, 30]. Fig.8a~b show the RRT distributions (normalized by the maximum RRT value) in PI and PII post-TEVAR, respectively. In PI, the highest RRT occurs at the FL proximal tip in PI-2~5; while in PI-6~7, RRT is greatly decreased and the highest RRT no longer occurs at the FL tip. In PII, the highest RRT also occurs at the FL proximal tip. Fig.8d displays the variation of the maximum RRT (normalized by the maximum RRT at the first follow-up, *i.e.* PI-2 and PII-2 for PI and PII respectively). The RRT variation in PI and PII shows significant difference during short-term follow-up: the normalized maximum RRT in PI increases greatly in PI-3 (from 1 to 5.516) and gradually decreases afterwards to 0.00405 in PI-7; while in PII, it decreases in PII-3 (from 1 to 0.025) and then maintains between 0.00324-0.319. The difference in the maximum RRT's variation pattern shows potential to predict different FL remodeling in the two patients.

DISCUSSION

Thoracic endografts, aiming to seal the primary entry and diverting blood flow into TL, are increasingly used in treating type-B aortic dissection[31]. Ideally, this approach would lead to thrombosis establishment in the FL and morphologic change in TL, to stabilize the aorta and consequently reduce aorta-related death. Previous studies confirmed the favorable results of TEVAR; however, also reported FL expansion on the segment distal to endografts, usually in the infrarenal aorta[32, 33]. This is related to the patency of FL[33] or, in other words, it is related to the flow field and hemodynamic conditions in AoD. Current literatures provide little information concerning the fate of the abdominal aorta post-TEVAR and, to our knowledge, computational studies on long-term multiple follow-up cases that are able to report the change of hemodynamic parameters have been lacking. Therefore, in the current study, we investigate two patients showing similar physical and hemodynamic features at initial presentation but presenting different FL development (stable in PI and expanded in PII) during the follow-ups. We preliminarily identify the possible hemodynamic parameters that could help to evaluate/predict FL enlargement and thrombosis formation. In this study, the variation trends of the hemodynamic parameters are more important than their absolute values.

The mechanical load acting on the FL boundary, which includes the outer wall of FL and the flap, induces FL enlargement and at the same time restricts TL remodeling. The pressure that is normally applied on the FL wall plays a key role in luminal remodeling[34] and the local flow directly relates to its distribution and magnitude. The flow can be assessed by its amount and the velocity. The first is mainly related to the size of tears. By comparing Fig.4b~c and Table 1, it can be found that the absolute flow mass passes each tear per second has positive relationship with the size of the tear. This can be shown on AoT-3 of PI and AoT-2~3 of PII, since they have multiple follow-up data, and it is consistent with previous report[14]. The second, velocity, is determined by both the flow rate as well as the tear size; a smaller tear size is correspondent to smaller flow rate yet accelerates the flow at the same time. For instance, in the final two examinations of PI (PI-6 and PI-7), the amount of the blood entering FL via AoT-3 decreases from 5.43% to 3.09% of the total flow and the tear size decreases from 93.49mm^2 to 44.09mm^2. However, the flow passing this tear has been accelerated and induces stronger impact on the FL outer wall (Fig.5e). If studying a longer period (PI-4~7), the variation of W_{FL} at L3 (Fig.2e), where just below AoT-3 in PI, is similar to the variation of the ratio between the diverted flow amount and the tear size.

Along the aorta, the pressure in TL decreases generally but that in FL, due to the vortical flow and its higher energy exchange, it does not present significant spatial difference. The AoTs, functioning as the bridge between TL and FL, transport blood flow and also pressure gradient. This induces similar pressure in the TL and FL near the tears. Because of the relatively uniform P_{FL} and its connection with P_{TL} at the tears, in general, P_{FL} is smaller than P_{TL} in the proximal region (above the AoTs) and higher than P_{TL} in the downstream. This general distribution feature is shown in Fig.5 in all of the post-interventional cases at the moment of systolic peak and similar patterns can be found in other time steps of the cardiac cycle.

At the flap, P_{FL} and P_{TL} conflict each other; the difference between them (PDiff) may be associated with subsequent luminal remodeling[14]. Luminal remodeling is a long-term effect; investigation of PDiff in short-term follow-ups may show the variation trends of lumen remodeling, while PDiff in long-term follow-ups may be consistent to lumen remodeling results. Indeed, taking L3 as an example, in short-term (PI-2~3, PII-2~3), PD in PII increases from 1.44 to 2.93mmHg (7days-1month);

while, PDiff in PI remains about 0.55mmHg (7days-4month). This, earlier than luminal change (Fig.2), shows the potential of FL enlargement for PII. In long-term follow-ups (PI-4~7, PII-4~5), AoT-3 becomes the main FL flow entry in PI and AoT-2 is the main entry in PII. PDiff increases from negative to positive slightly below the position of AoT-3 in PI and AoT-2 in PII. Moreover, in both patients, in the final examination, the maximum PDiff occurs near L3, where W_{FL} increases the most (among the compared four positions) and W_{TL} in PII decreases. The abovementioned indicates: (i) in short-term follow-ups, great increase of PDiff may imply potential FL expansion; (ii) while, in long-term follow-up, the position of the first flow entry of FL is the negative-to-positive watershed of PDiff, the position of the maximum PDiff is consistent with the greatest W_{FL} increase, and when the maximum PDiff is small (0.22mmHg in PI-7), the pressure induces slight FL expansion without restricted acts on TL, but when it is relatively large (1.39mmHg in PII-5), both FL expansion and TL collapse are found. In clinical examinations, monitoring PDiff at early-stage and identifying the position of FL entries and the position of largest PDiff may assist in wisely control of the untreated aorta segment.

The WSS is related to the formation of thrombosis. Previous studies suggested that the tearing of the aortic wall and high WSS in the near region of the tears could promote initial activation of platelets as well as the formation of platelet aggregates; while, the highly vortical flow pattern in the FL corresponding with low WSS promotes platelet aggregation and deposition, so that leads to surface thrombosis [35, 36]. In other words, lower WSS may induce surface thrombus and thus lead to constructive FL remodeling [37, 38]. In the long-term follow-ups (PI-4~5 and PII-4~5), complete thrombosis is found at the proximal region of dissection and partial thrombosis remains above the re-entries. The partial thrombosis in both PI and PII is aligned with the intimal flap; thus, WSS on the flap along the TL and FL sides are compared. The WSS_{FL} is significantly lower than WSS_{TL} throughout the cardiac cycle; the low WSS_{FL} possibly induces surface thrombus along the flap in FL while the high WSS_{TL} can keep the TL patent. The lowest WSS_{FL} (<0.25Pa) occurs at the proximal region of FL (Fig.7d), implying potential thrombosis in these regions. Indeed, partial thrombosis in PI-4~5 with very low WSS_{FL} turns to complete thrombosis in PI-6~7 (indicated by arrow inFig.7d). Moreover, in PII, the WSS_{FL} at the tip of the flap in PII-3 is small (<0.25Pa). In its next follow-up (PII-4), growth of partial thrombosis can be found (indicated by arrow in Fig.7d). However, slightly higher WSS_{FL} is shown in PII-4 at the proximal tip, and in its next follow-up (PII-5), the partial thrombosis is slightly reduced (indicated by hollow arrow in Fig.7d). This indicates the surface thrombosis is possibly very sensitive to WSS, and during the long-term recovery, FL regression/growth could be repeatedly occurred at the proximal tip of the FL.

The derived parameter of shear stress - RRT is related to particle residence and may reflect thrombosis establishment as well[14]. To identify the location of high RRT, Fig.8a~b draw the distribution of the normalized RRT to its maximum value in each model. It shows that high RRT corresponds to the region with highly vortical and low velocity flow. This occurs at the FL proximal tip for both the patients (PI-2~5, PII-2~5). Moreover, Fig.8ccompares the magnitude of RRT in PI-5 and PII-4, in which the follow-up periods are similar (21 and 18months for PI and PII respectively). The maximum RRT in PI-5 and PII-4 are 68.94 and $70.66Pa^{-1}$ respectively. The similar distribution pattern and magnitude of RRT in PI and PII indicates that the values of RRT alone may not be able to predict FL remodeling. To further investigate this, the variation of the maximum RRT is studied (Fig.8d). The maximum RRTs in PI-3~7 and PII-3~5 are normalized to the correspondent first follow-up results (PI-2 and PII-2, 7days post-TEVAR). The variation patterns of this normalized maximum RRT show significant difference between PI and PII. This implicates that, post-TEVAR, variation of RRT in short- to middle-term follow-up (PI-2~5, PII-2~4) may play a key role in thrombosis establishment: an increase of RRT after TEVAR and maintaining the relative normalized maximum RRT value to be above 1.0 (Fig.8d) may lead to positive FL remodeling.

Common morphological predictors for re-intervention or surgery after TEVAR include aortic diameter >55mm and growth rate >10mm/year [39]. Hemodynamic condition of the dissected aorta plays an important role in driving TL and FL remodeling. In other words, hemodynamic parameters may have the potential to predict the dissection development earlier than morphological change. However, hemodynamic markers that can possibly predict FL development post-TEVAR have not been proposed yet, which would require long-term multiple follow-up analyses. The current study investigated the correlation of hemodynamic parameters to the development of post-TEVAR dissection. It preliminarily proposed the parameters that are potential to differentiate the enlarged and stable FL in an early stage post-TEVAR. Although this study was based on a limited number of patient cases and thus no clinical conclusion can be drawn at this stage, it is the basis to future studies on a larger amount of patient cases and would contribute to the research regarding early decision-making on re-intervention or surgery for AoD after TEVAR.

LIMITATIONS

This study, based on long-term multiple follow-up data of two patients, preliminarily shows the relationship of the variations between hemodynamic parameters and luminal remodeling. However, critical values of these parameters should be better determined by involving a greater number of patient cases. Besides, more detailed mechanical analysis should involve the fluid-structure interaction analysis, which does not only provide the stress information in the aortic wall but also offer more accurate results on the WSS. However, due to the complex geometry and the lack of the actual material properties, the existed fluid-structure interaction studies on AoD often generate the aortic/dissection wall with arbitrary thickness and assume the mechanical properties of the aortic and dissection wall similar to the properties of aortic aneurysms. More accurate simulations are highly dependent on accurate model establishment and material property measurements, which are currently carried on in our laboratory.

ACKNOWLEDGEMENTS

This study was supported by National Natural Science Foundation of China (81471752, 81353265), National Science and Technology Pillar Program of China (2015BAI04B03), and National Key Research and Development Program of China (2017YFC0107900). PW was partially supported by UK EPSRC (EP/N014642/1).

CONFLICTS OF INTEREST

No

ETHICAL APPROVAL

This study was approved by the Institutional Review Board of Chinese PLA General Hospital (ref no. 20110903.V1.1)

REFERENCES

1. Younes, H.K., P.W. Harris, J. Bismuth, K. Charlton-Ouw, E.K. Peden, A.B. Lumsden, and M.G. Davies, Thoracic endovascular aortic repair for type B aortic dissection. Ann Vasc Surg 2010; 24: p. 39-43.
2. Weber, T.F., D. Bockler, M. Muller-Eschner, M. Bischoff, M. Kronlage, H. von Tengg-Kobligk, H.U. Kauczor, and A. Hyhlik-Durr, Frequency of abdominal aortic expansion after thoracic endovascular repair of type B aortic dissection. Vascular 2016; 24: p. 567-79.
3. Doyle, B.J. and P.E. Norman, Computational Biomechanics in Thoracic Aortic Dissection: Today's Approaches and Tomorrow's Opportunities. Ann Biomed Eng 2016; 44: p. 71-83.
4. Saad, A.A., T. Loupas, and L.G. Shapiro, Computer vision approach for ultrasound Doppler angle estimation. J Digit Imaging 2009; 22: p. 681-88.
5. Muller-Eschner, M., F. Rengier, S. Partovi, R. Unterhinninghofen, D. Bockler, S. Ley, and H. von Tengg-Kobligk, Tridirectional phase-contrast magnetic resonance velocity mapping depicts severe hemodynamic alterations in a patient with aortic dissection type Stanford B. J Vasc Surg 2011; 54: p. 559-62.
6. Stadlbauer, A., W. van der Riet, S. Globits, G. Crelier, and E. Salomonowitz, Accelerated phase-contrast MR imaging: comparison of k-t BLAST with SENSE and Doppler ultrasound for velocity and flow measurements in the aorta. J Magn Reson Imaging 2009; 29: p. 817-24.
7. Kohler, B., U. Preim, M. Grothoff, M. Gutberlet, K. Fischbach, and B. Preim, Motion-aware stroke volume quantification in 4D PC-MRI data of the human aorta. Int J Comput Assist Radiol Surg 2016; 11: p. 169-79.
8. Sakalihasan, N., C.A. Nienaber, R. Hustinx, P. Lovinfosse, M. El Hachemi, J.P. Cheramy-Bien, L. Seidel, J.P. Lavigne, J. Quaniers, M.A. Kerstenne, A. Courtois, A. Ooms, A. Albert, J.O. Defraigne, and J.B. Michel, (Tissue PET) Vascular metabolic imaging and peripheral plasma biomarkers in the evolution of chronic aortic dissections. Eur Heart J Cardiovasc Imaging 2015; 16: p. 626-33.
9. Nchimi, A., J.P. Cheramy-Bien, T.C. Gasser, G. Namur, P. Gomez, L. Seidel, A. Albert, J.O. Defraigne, N. Labropoulos, and N. Sakalihasan, Multifactorial relationship between 18F-fluoro-deoxy-glucose positron emission tomography signaling and biomechanical properties in unruptured aortic aneurysms. Circ Cardiovasc Imaging 2014; 7: p. 82-91.
10. Alimohammadi, M., O. Agu, S. Balabani, and V. Diaz-Zuccarini, Development of a patient-specific simulation tool to analyse aortic dissections: assessment of mixed patient-specific flow and pressure boundary conditions. Med Eng Phys 2014; 36: p. 275-84.
11. Karmonik, C., M. Muller-Eschner, S. Partovi, P. Geisbusch, M.K. Ganten, J. Bismuth, M.G. Davies, D. Bockler, M. Loebe, A.B. Lumsden, and H. von Tengg-Kobligk, Computational fluid dynamics investigation of chronic aortic dissection hemodynamics versus normal aorta. Vasc Endovascular Surg 2013; 47: p. 625-31.
12. Shang, E.K., D.P. Nathan, R.M. Fairman, J.E. Bavaria, R.C. Gorman, J.H. Gorman, 3rd, and B.M. Jackson, Use of computational fluid dynamics studies in predicting aneurysmal degeneration of acute type B aortic dissections. J Vasc Surg 2015; 62: p. 279-84.
13. Tse, K.M., P. Chiu, H.P. Lee, and P. Ho, Investigation of hemodynamics in the development of dissecting aneurysm within patient-specific dissecting aneurismal aortas using computational fluid dynamics (CFD) simulations. J Biomech 2011; 44: p. 827-36.
14. Cheng, Z., N.B. Wood, R.G. Gibbs, and X.Y. Xu, Geometric and flow features of type B aortic dissection: initial findings and comparison of medically treated and stented cases. Ann Biomed Eng 2015; 43: p. 177-89.
15. Chen, D., M. Muller-Eschner, H. von Tengg-Kobligk, D. Barber, D. Bockler, R. Hose, and Y. Ventikos, A patient-specific study of type-B aortic dissection: evaluation of true-false lumen blood exchange. Biomed Eng Online 2013; 12: p. 65.
16. Karmonik, C., J. Bismuth, M.G. Davies, D.J. Shah, H.K. Younes, and A.B. Lumsden, A computational fluid dynamics study pre- and post-stent graft placement in an acute type B aortic dissection. Vasc Endovascular Surg 2011; 45: p. 157-64.
17. Cheng, S.W., E.S. Lam, G.S. Fung, P. Ho, A.C. Ting, and K.W. Chow, A computational fluid dynamic study of stent graft remodeling after endovascular repair of thoracic aortic dissections. J Vasc Surg 2008; 48: p. 303-9.
18. Chen, D., M. Muller-Eschner, D. Kotelis, D. Bockler, Y. Ventikos, and H. von Tengg-Kobligk,

A longitudinal study of Type-B aortic dissection and endovascular repair scenarios: computational analyses. Med Eng Phys 2013; 35: p. 1321-30.

19. Karmonik, C., J. Bismuth, D.J. Shah, M.G. Davies, D. Purdy, and A.B. Lumsden, Computational study of haemodynamic effects of entry- and exit-tear coverage in a DeBakey type III aortic dissection: technical report. Eur J Vasc Endovasc Surg 2011; 42: p. 172-7.
20. Naim, W.N.W.A., P. Ganesan, Z. Sun, K. Osman, and E. Lim, The impact of the number of tears in patient-specific stanford type B aortic dissecting aneurysm: CFD simulations. J Mech Med Biol 2014; 14: p. 1450017.
21. Alimohammadi, M., J.M. Sherwood, M. Karimpour, O. Agu, S. Balabani, and V. Diaz-Zuccarini, Aortic dissection simulation models for clinical support: fluid-structure interaction vs. rigid wall models. Biomed Eng Online 2015; 14: p. 34.
22. Qiao, A., W. Yin, and B. Chu, Numerical simulation of fluid-structure interaction in bypassed DeBakey III aortic dissection. Comput Methods Biomech Biomed Engin 2015; 18: p. 1173-80.
23. Clough, R.E., V.E. Zymvragoudakis, L. Biasi, and P.R. Taylor, Usefulness of new imaging methods for assessment of type B aortic dissection. Ann Cardiothorac Surg 2014; 3: p. 314-8.
24. Birjiniuk, J., J.M. Ruddy, E. Iffrig, T.S. Henry, B.G. Leshnower, J.N. Oshinski, D.N. Ku, and R.K. Veeraswamy, Development and testing of a silicone in vitro model of descending aortic dissection. J Surg Res 2015; 198: p. 502-7.
25. Soudah, E., P. Rudenick, M. Bordone, B. Bijnens, D. Garcia-Dorado, A. Evangelista, and E. Onate, Validation of numerical flow simulations against in vitro phantom measurements in different type B aortic dissection scenarios. Comput Methods Biomech Biomed Engin 2015; 18: p. 805-15.
26. Vignon-Clementel, I.E., C.A. Figueroa, K.E. Jansen, and C.A. Taylor, Outflow boundary conditions for three-dimensional finite element modeling of blood flow and pressure in arteries. Comput Methods Biomech Biomed Engin 2006; 195: p. 3776-96.
27. Ganten, M.K., T.F. Weber, H. von Tengg-Kobligk, D. Bockler, W. Stiller, P. Geisbusch, G.W. Kauffmann, S. Delorme, M. Bock, and H.U. Kauczor, Motion characterization of aortic wall and intimal flap by ECG-gated CT in patients with chronic B-dissection. Eur J Radiol 2009; 72: p. 146-53.
28. Papaharilaou, Y., D.J. Doorly, and S.J. Sherwin, The influence of out-of-plane geometry on pulsatile flow within a distal end-to-side anastomosis. J Biomech 2002; 35: p. 1225-39.
29. Bortolotto, L.A. and M.E. Safar, Blood pressure profile along the arterial tree and genetics of hypertension. Arq Bras Cardiol 2006; 86: p. 166-9.
30. Gorring, N., L. Kark, A. Simmons, and T. Barber, Determining possible thrombus sites in an extracorporeal device, using computational fluid dynamics-derived relative residence time. Comput Methods Biomech Biomed Engin 2015; 18: p. 628-34.
31. Nienaber, C.A., S. Kische, H. Ince, and R. Fattori, Thoracic endovascular aneurysm repair for complicated type B aortic dissection. J Vasc Surg 2011; 54: p. 1529-1533.
32. Andacheh, I.D., C. Donayre, F. Othman, I. Walot, G. Kopchok, and R. White, Patient outcomes and thoracic aortic volume and morphologic changes following thoracic endovascular aortic repair in patients with complicated chronic type B aortic dissection. J Vasc Surg 2012; 56: p. 644-50.
33. Sigman, M.M., O.P. Palmer, S.W. Ham, M. Cunningham, and F.A. Weaver, Aortic morphologic findings after thoracic endovascular aortic repair for type B aortic dissection. JAMA Surg 2014; 149: p. 977-83.
34. Sueyoshi, E., I. Sakamoto, K. Hayashi, T. Yamaguchi, and T. Imada, Growth rate of aortic diameter in patients with type B aortic dissection during the chronic phase. Circulation 2004; 110: p. II256-61.
35. Sheriff, J., D. Bluestein, G. Girdhar, and J. Jesty, High-shear stress sensitizes platelets to subsequent low-shear conditions. Ann Biomed Eng 2010; 38: p. 1442-50.
36. Goel, M.S. and S.L. Diamond, Adhesion of normal erythrocytes at depressed venous shear rates to activated neutrophils, activated platelets, and fibrin polymerized from plasma. Blood 2002; 100: p. 3797-803.
37. Wu, M.H., Y. Kouchi, Y. Onuki, Q. Shi, H. Yoshida, S. Kaplan, R.F. Viggers, R. Ghali, and L.R. Sauvage, Effect of differential shear stress on platelet aggregation, surface thrombosis, and endothelialization of bilateral carotid-femoral grafts in the dog. J Vasc Surg 1995; 22: p. 382-90.

38. Menichini, C., Z. Cheng, R.G. Gibbs, and X.Y. Xu, Predicting false lumen thrombosis in patient-specific models of aortic dissection. J R Soc Interface 2016; 13: p. 20160759.
39. Erbel, R., V. Aboyans, C. Boileau, E. Bossone, R.D. Bartolomeo, H. Eggebrecht, A. Evangelista, V. Falk, H. Frank, O. Gaemperli, M. Grabenwoger, A. Haverich, B. Iung, A.J. Manolis, F. Meijboom, C.A. Nienaber, M. Roffi, H. Rousseau, U. Sechtem, P.A. Sirnes, R.S. Allmen, and C.J. Vrints, 2014 ESC Guidelines on the diagnosis and treatment of aortic diseases: Document covering acute and chronic aortic diseases of the thoracic and abdominal aorta of the adult. The Task Force for the Diagnosis and Treatment of Aortic Diseases of the European Society of Cardiology (ESC). Eur Heart J 2014; 35: p. 2873-926.

FIGURE LEGENDS

Fig.1 (a)~(d) display the reconstructed models of AoD (D-days, M-months); (e) is a sonogram of Doppler ultrasound velocimetry, the upper edge of which is shown in green; (f) shows an axial slice of CTA scan at initial presentation of PI, in which the segmented lumen boundary is shown in yellow.

Fig.2 The luminal remodeling. (a) displays the measured axial positions (L1-4) and the regions to calculate luminal volume (V_{TL}, V_{TL} -Part and V_{FL}); (b)~(e) show the variation of luminal volume, aortic diameter, width of TL and FL respectively.

Fig.3 Flow patterns of AoD. (a)~(b) display the flow streamlines at systolic peak; (c) shows the streamlines at the proximal region of FL in the final model of PII.

Fig.4 Flow exchange between the true and false lumen. (a) displays the variation of the mass flow rate towards the FL via the primary entry, AoT-2 and AoT-3 over a cardiac cycle at initial presentation; (b) and(c) respectively show the mass flow rate variation at AoT-2 and AoT-3 during the longitudinal follow-ups.

Fig.5 Pressure distribution along the dissected aorta. (a) and (b) display the PDsys distribution in PI and PII respectively; (c) shows the PDsys in a normal aorta; (d) displays the variation of the maximum PDsys during the follow-up; (e) shows the Psys at a slice crossing the FL in the final two examinations of PI and in the final examination of PII; and (f) shows the region with Psys$\geqslant$ 09.15mmHg (in red).

Fig.6 Pressure difference between FL and TL for PI (a)~(d) and PII (e)~(f).

Fig.7 WSS distribution along the flap. (a) and (b) display the WSS distribution at systolic peak on the flap of TL and FL side respectively; (c) and (d) show the WSS distribution on the flap of FL side during the long-term follow-ups in different WSS ranges.

Fig.8 RRT distribution and variation. (a) and (b) show the normalized RRT to its maximum value post-TEVAR in PI and PII respectively; (c) shows the RRT distribution at PI-5 and PII-4, where the follow-up periods in PI and PII are similar; and (d) displays the variation of the normalized maximum RRT to its value in the first follow-up (PI-2 for PI and PII-2 for PII).

Hemodynamic Parameters That May Predict False-lumen Growth in Type-B Aortic Dissection after Endovascular Repair: A Preliminary Study on Long-term Multiple Follow-ups

Huanming Xu[1,2], Zhenfeng Li[1,2], Huiwu Dong[3], Yilun Zhang[1], Jianyong Wei[1], Paul N. Watton[5,6], Wei Guo[7], Duanduan Chen[1,2]*, Jiang Xiong[7]*

[1]School of Life Science, Beijing Institute of Technology, China
[2]Key Laboratory of Convergence Medical Engineering System and Healthcare Technology, The Ministry of Industry and Information Technology, Beijing Institute of Technology, China
[3]Department of Ultrasound Diagnosis, Chinese PLA General Hospital, China
[5]Department of Computer Science & INSIGNEO Institute, University of Sheffield, UK
[6]Department of Mechanical Engineering and Material Science, University of Pittsburgh
[7]Department of Vascular and Endovascular Surgery, Chinese PLA General Hospital, China

***Corresponding author:** Prof Duanduan Chen
School of Life Science, Beijing Institute of Technology, Beijing,
100081, China.
Tel. +86-10-68912154
Email. duanduan@bit.edu.cn

Dr Jiang Xiong
Department of Vascular and Endovascular Surgery,
Chinese PLA General Hospital, Beijing, 100853, China.
Tel. +86-10-66938349
Email. xiongjiangdoc@126.com

ABSTRACT

Thoracic endovascular aortic repair (TEVAR) is commonly applied in type-B aortic dissection. For patients with dissection affects descending aorta and extends downward to involve abdominal aorta and possibly iliac arteries, false lumen (FL) expansion might occur post-TEVAR. Predictions of dissection development may assist in medical decision on re-intervention or surgery. In this study, two patients are selected with similar morphological features at initial presentation but with different long-term FL development post-TEVAR (stable and enlarged FL). Patient-specific models are established for each of the follow-ups. Flow boundaries and computational validations are obtained from Doppler ultrasound velocimetry. By analyzing the hemodynamic parameters, the false-to-true luminal pressure difference (PDiff) and particle relative residence time (RRT) are found related to FL remodeling. It is found that (i) the position of the first FL flow entry is the watershed of negative-and-positive PDiff and, in long-term follow-ups, and the position of largest PDiff is consistent with that of the greatest increase of FL width; (ii) high RRT occurs at the FL proximal tip and similar magnitude of RRT is found in both stable and enlarged cases; (iii) comparing to the RRT at 7days post-TEVAR, an increase of RRT afterwards in short-term is found in the stable case while a slight decrease of this parameter is found in the enlarged case, indicating that the variation of RRT in short-term post-TEVAR might be potential to predict long-term FL remodeling.

Key Words: aortic dissection; hemodynamics; endovascular procedures.

INTRODUCTION

Aortic dissection (AoD) is a severe cardiovascular disease, where a surge of blood flowing into the aortic wall via an initial tear or damage of the intima and splitting the single aortic lumen into a true and false lumen (TL and FL). Stanford type-B AoD indicates those with the dissection begins distal to the supraaortic branches. Interventional treatment of Stanford type-B AoD commonly involves thoracic endovascular aortic repair (TEVAR)[1]. In a number of patients, FL expansion is found post-TEVAR, especially in the infrarenal aorta. Recent study confirmed that abdominal aortic expansion can be frequently found after TEVAR and is independent from thoracic FL thrombosis[2]. Prediction of FL growth may contribute to early decision-making of re-intervention or surgery. The post-TEVAR development of dissection is highly dependent on local hemodynamics[3]. Medical imaging tools such as Doppler ultrasound[4] and phase-contrast MR (pcMR)[5] are able to capture the flow velocity within aorta. However, the former provides velocity information at a certain position of the vessel, and the latter reveals flow movement with relatively low spatial and temporal resolution[6, 7]. On the other hand, the uptake of ^{18}F-fluorodeoxyglucose in PET-CT can indicate complications in AoD[8] and positive correlation between the uptake and wall shear stress is found in aortic aneurysm study[9]; however, PET-CT is relatively expensive and the flow information cannot be directly reported. Thus, computational simulations that can provide hemodynamic parameters, such as flow, pressure and shear stress distributions, may enrich analysis.

Previous computational works focusing on type-B AoD include investigations on hemodynamic features[10-14], luminal flow exchange[12, 15], post-TEVAR flow effects[16-18], tear-induced flow effects[19, 20] and fluid-structure interaction studies[21, 22]. Besides, 4D pcMR[5, 23] and phantom[24, 25] measurements have been conducted to compare with or validate the computed results. In this study, we investigate the flow-driven dissection development after TEVAR based on long-term multiple follow-ups. Flow conditions in patients with stable and enlarged FL are compared and key hemodynamic parameters that are related to dissection growth in abdominal aorta are proposed, facilitating medical decision-making on post-TEVAR treatment.

METHODS

Image Acquisition and Model Reconstruction

This study was approved by the institutional review board of the Chinese PLA General Hospital. Written informed consent was obtained from the patients involved in this study. Two male patients (PI and PII) with subacute Stanford type-B AoD underwent arterial-phase CT angiography (CTA) at initial presentation and during the follow-up examinations after TEVAR via a dual-source CT scanner (SOMATOM Definition Flash, SIEMENS, Germany). Details of the CTA scan and the patient information are described in S1, Supporting Document. Image segmentation and surface reconstruction of AoD were conducted through Mimics (Materialise, Belgium). The cross-sectional contours of the reconstructed geometries were mapped back to CTA images to ensure that the 3D models present the actual outline of the vessel lumen. Detailed views of the models are shown in Fig.1, where PI/II-1 indicates the models pre-TEVAR while PI/II-2 and others are models post-TEVAR. After TEVAR, PI and PII have experienced six- (7days~53months) and four-times (7days~35months) CTA scans. The FL in PI was in stable condition (PI-2~7, Fig.1b) while that in PII was expanding (PII-2~5, Fig.1d). The models were meshed in ICEM (ANSYS Inc, Canonsburg, USA) with tetrahedral elements in the core region and prismatic cells (10 layers) in the boundary layer near the aortic wall. The grid resolution varies from 2,564,019 to 3,153,829 cells.

Doppler Ultrasound and Boundary Conditions

Time-variant velocities at ascending aorta (AAo), brachiocephalic trunk (BT), left common carotid artery (LCCA), left subclavian artery (LSA) were measured via Doppler ultrasound of the patients, and velocity variation at the distal thoracic aorta (DTAo, about 5cm above celiac trunk) was measured in the final examination of PI to provide validation of the computational results. This is because the true lumen (TL) remodeling at this position in PI is sufficient, so that relatively organized flow is found and the central line of vessel can be accurately identified. The velocity of AAo was measured through the apical 5-chamber view and the suprasternal long axis view of aortic arch. The two results were compared to ensure the maximum velocity at AAo could be captured. For other arteries (BT, LCCA, LSA and DTAo), Doppler velocimetry has been conducted at the proximal and distal sites of the targeted measurement vessel. Mean velocity over a cardiac cycle at the two sites for each particular vessel was then calculated and compared. When the difference between them is less than 5%, the measured velocity is considered effective. Details of the measurement are described in S2, Supporting Document.

The upper edge of the velocity sonogram was extracted (Fig.1e) as the variation of the maximum velocity at the measured site. The flow rates at AAo, BT, LCCA and LSA, as the velocity boundary conditions, can then be calculated based on the measured time-variant maximum velocity and the assumed flat flow profile for AAo and parabolic flow profile for the others. The velocity boundary conditions of the models is shown in Fig.S1a, Supporting Document. Pulsatile waveforms of the pressure at celiac artery (CA), superiormesenteric artery (SMA), renal arteries and the outlets at common iliac arteries were obtained from previous study[26] (Fig.S1b, Supporting Document). As shown in Fig.1, two models in PII (PII-1 and PII-4) were cropped below the iliac bifurcation due to the relatively shorter CT scanning range. To eliminate the outlet effects, time-variant pressure distribution at the cropping plane has been calculated in PII-2~3 and PII-5. The averaged pressure information at this cropping plane was mapped to PII-1 and PII-4, serving as the pulsatile pressure outlets.

Numerical Models

The vessel wall was assumed as no-slip and rigid, due to low distensibility in long-term follow-ups[27]. The blood was treated as Newtonian and incompressible with density of 1044kg/m^3 and dynamic viscosity of 0.00365kg·m^{-1}·s^{-1}[28]. The average Reynolds number over a cardiac cycle, calculated based on the equivalent diameter ($D_e = 2\sqrt{Area/\pi}$) and velocity at the inlet of the ascending aorta in PI and PII, were between 2066-2197 and 2844-2960, respectively. Our previous study confirmed that laminar simulations with adequately fine mesh resolutions, especially refined near the walls, can capture flow patterns as turbulence model[15]. To further confirm this, we solved the flow in the first follow-up cases (PI-2 and PII-2) by both laminar and k-ω SST turbulence models, where the flow in the abdominal aortic region is the fastest during the follow-ups. Similar flow patterns were found and the discrepancy of the maximum velocity and wall shear stress (WSS) in the abdominal aorta was 4.2% and 5.2% respectively (the laminar and turbulent results of PII-2 were shown in Fig.S2, Supporting Document), ensuring the rationality of laminar model to be applied in the current problem. A finite volume solver, CFD-ACE+ (ESI Group, France) was employed. The heart-beat cycle of the patients was measured at each clinical examination. The averaged cardiac cycle for PI and PII were 71 and 69beat/min respectively. Temporal discretization of numerical models was assigned as 45step/cycle. Simulation was carried out for 5 cardiac cycles to achieve a periodic solution and results of the final cycle were presented. Grid and temporal independency analyses on finer grids and finer temporal discretizations were conducted to ensure the base resolution with the base time step settings are adequate (S3, Supporting Document).

RESULTS

Aortic Remodeling

Aortic remodeling was assessed by: (i) size and numbers of the aortic tears (AoT), (ii) change of luminal volume, and (iii) growth of aortic diameter. There are four major AoTs along the aorta for both patients at initial presentation. The primary entry (AoT-1) in both patients is located at the proximal region of descending aorta and the locations of other AoTs (AoT-2~4) are displayed in Fig.1. After TEVAR, the primary entry was sealed and after the first follow-up of PI, AoT-2 was disappeared. Considering the position and local aortic curvature of the tears, AoT-4 is the exit of the flow from FL to TL, while the function of AoT-2 and AoT-3 is uncertain. Since only the flow entries towards the FL is able to bring mechanical impact into the dissection, size measurement was only performed on AoT-2 and AoT-3 (Table 1). Post-TEVAR, both AoT-2 and AoT-3 in PI and PII are enlarged, probably due to the greater flow impact on these sites after AoT-1 was sealed.

Table 1. The size of the aortic tears in the patients with long-term follow-ups

Tear	Geometry	PI-1	PI-2	PI-3	PI-4	PI-5	PI-6	PI-7
AoT-2	H[mm]	7.87	7.15	-	-	-	-	-
	W[mm]	8.97	10.76	-	-	-	-	-
	A[mm^2]	64.61	70.71	-	-	-	-	-
AoT-3	H[mm]	13.86	18.79	17.93	15.31	18.23	8.81	8.57
	W[mm]	10.04	9.38	6.03	8.90	7.30	6.72	5.75
	A[mm^2]	116.13	150.82	106.40	119.19	128.82	93.49	44.09

Tear	Geometry	PII-1	PII-2	PII-3	PII-4	PII-5
AoT-2	H[mm]	8.17	8.41	5.74	11.04	11.20
	W[mm]	9.34	9.96	7.36	9.59	6.03
	A[mm^2]	62.61	70.47	37.33	89.50	54.05
AoT-3	H[mm]	9.91	9.55	7.77	6.25	6.19
	W[mm]	10.01	11.47	9.34	8.04	9.90
	A[mm^2]	85.27	99.32	61.51	40.35	53.32

H-Height; W-Width; A-Area.

The change of luminal volume is shown in Fig.2. The volume of TL (V_{TL}) involves the initial dissection-affected TL region, while $V_{TL\text{-}Part}$ indicates the dissection-affected TL region during the follow-ups. Variations of V_{TL}, volume of FL (V_{FL}) and the ratio between $V_{TL\text{-}Part}$ and V_{FL} are displayed in Fig.2b. V_{FL} in the stable case (PI) reduces gradually post-TEVAR, except for the final examination, where a trivial increase of V_{FL} is found (131.6mm^3 in 20months). However, V_{FL} in the expanding case (PII) reduces in the first two follow-ups but enlarges afterwards, where the V_{FL} growths in PII-4 and PII-5 are 2,138mm^3 and 34,989mm^3 respectively, the durations of which are both 17months (Fig.2b). For both cases, the TL-to-FL volume ratio ($V_{TL\text{-}Part}/V_{FL}$) keeps increasing, except for PI-6 and PII-3 (pointed by arrows). This is because significant FL regression occurs at the proximal region (blue squares in Fig.1b,1d), which shortens the comparison region. Since TL remodeling is insufficient in this region, value of $V_{TL\text{-}Part}/V_{FL}$ reduces. The averaged increase rates of $V_{TL\text{-}Part}/V_{FL}$ in the follow-ups of PI and PII are 1.8% and 0.3% per month, respectively, indicating a significant luminal remodeling difference.

The aortic diameter (D) is measured in each model, taking into account the width of TL and FL (W_{TL} and W_{FL}) and the thickness of flap. As shown in Fig.1f, measurements have been conducted in the axial plane of the CTA datasets, along a line that crosses the centre of the flap and is perpendicular to the flap. Four measurement positions are selected in the abdominal aorta. As shown in Fig.2a, they are 1cm below diaphragm (L1), 1cm above CA (L2), 3.5cm below SMA (L3) and 9cm below SMA (L4). Fig.2c~e display the variation of D, W_{TL} and W_{FL} respectively. Positive TL remodeling is found in PI and PII in general, except for L3 and L4 in PI-3 and L3 in PII-4~5. W_{FL} at the proximal region of PI (L1 and L2) reduces greatly during the follow-up, while in the distal region (L3 and L4), variation of W_{FL} is stable. In PII, W_{FL} increases sharply since the second follow-up (PII-3). Comparing the variation of W_{TL}, W_{FL} and D, it can be found that the variation pattern of D is mainly determined by the variation of W_{FL}.

Flow Pattern, Validation and Luminal Flow Exchange

Fig.3 shows the flow streamlines at systolic peak where the color map of velocity magnitude is restricted to a certain range in PI (0~2.51m/s) and PII (0~3.78m/s) to assist visualization of the longitudinal velocity variation. At systolic peak, fast and organized flow is found in TL; while vortical and relatively slow flow presents in FL. Highest velocity presents in the short-term follow-ups (PI-2~3, 4months for PI; PII-2~3, 1months for PII) at the region below stentgraft and above AoT-2 and -3, where TL remodeling is insufficient and the blood has not been diverted. In long-term follow-ups (PI-4~7 and PII-4~5), the flow in the proximal FL is generally slow (<0.5mm/s); while below AoT-2 (the first re-entry), where blood perfusion occurs, faster flow up to 1.53m/s in PI and 2.22m/s in PII are found in the FL with helical feature (Fig.3c).

To validate the computational results, Doppler ultrasound velocimetry was performed at distal thoracic aorta (5cm above CA) along the centerline of TL. This was only conducted at the final examination of PI, because its TL in the distal thoracic aorta is fully remodeled and the local flow is therefore organized (Fig.3a). The measured and computed velocities at the centre of the cross-section of the vessel, 5cm above CA, are 1.58m/s and 1.66m/s respectively, indicating a difference of 5.1%. Moreover, the computed velocity variation pattern is similar to the measured one (Fig.S3, Supporting Document), ensuring the rationality of computational results.

Fig.4 displays the luminal flow exchange via the primary entry for initial presentation and that via AoT-2 and AoT-3 during the follow-ups. As abovementioned, AoT-4 functions as the outlet of FL throughout the cardiac cycle, thus it is not displayed in Fig.4. As shown in Fig.4a (positive values indicates flow enters FL), before treatment, the TL-to-FL flow exchange in PI and PII presents similar pattern: the primary entry serves as the main flow inlet of FL; AoT-2 functions as the outlet of FL in the initial part of systole and behaves as inlet in the rest part of cardiac cycle; and AoT-3 mainly serves as the outlet of FL. There are 31.48% and 40.00% of the total flow diverted to FL over a cardiac cycle for PI and PII respectively, at initial presentation. After TEVAR, the function of the tears changes. In PI, AoT-2 becomes the inlet of FL in the entire heart-beat cycle (Fig.4b), while AoT-3 functions as the inlet of FL during systole and serves as the outlet in diastole (Fig.4c). Since the second follow-up of PI, AoT-2 is closed and AoT-3 gradually becomes the inlet of FL throughout the entire cardiac cycle. The flow entering FL are 16.67%, 6.98%, 8.24%, 9.59%, 5.43%, 3.09% of the total flow for case PI-2~7 respectively, the variation of which is consistent to the variation of tear size (Table 1) and it is generally reducing. In PII, both of AoT-2 and AoT-3 are existed during the follow-ups. AoT-2 mainly serves as the inlet of FL; especially in model PII-4 and PII-5, positive values of mass flow rate are found in the entire cardiac cycle (Fig.4b). AoT-3 diverts a small amount of flow into the FL during systole and mainly behaves as the outlet of FL (Fig.4c). There are 5.22%, 3.06%, 14.76% and 10.23% of the total flow diverted into FL in case PII-2~5 respectively, the variation of which is also consistent with the variation of tear size.

Loading Distribution along the Aorta

Fig.5a~b display the pressure drop at systolic peak (PDsys, the difference between the local pressure and the pressure at the bottom of the model). In TL, PDsys reduces from the inlet of AAo to the outlets of common iliac arteries. At initial presentation (PI-1 and PII-1), FL diverts part of the total flow (31.48% for PI and 40.00% for PII), maintaining PDsys in relatively low values. After TEVAR, in short-term follow-ups (PI-2~3 and PII-2~3), proximal descending aorta is supported by stentgraft and reshaped; however, below the endograft, TL remains collapsed, inducing larger resistance and resulting in higher velocity and regional lower pressure in this region (indicated by arrows in Fig.5a~b). In long-term follow-ups (PI-4~7 and PII-4~5), TL remodeling in distal thoracic aorta is improved; PDsys thus gradually reduces along aorta. In contrary, PDsys in FL is relatively uniform, which is probably due to the higher energy exchange induced by the vortical flow. Fig.5d shows the variation of the maximum PDsys during the follow-ups. For both patients, the maximum PDsys increases greatly soon after TEVAR (7days); along with the progress of TL remodeling, the maximum PDsys reduces. The PDsys in normal aorta model (Fig.5c) based on the same boundary conditions as PI and PII is also computed and the averaged maximum PDsys is shown by the dash line in Fig.5d. Since the growth of FL in the two patients shows obvious difference, the similar variation pattern of PDsys indicates that the pressure drop is mainly affected by TL remodeling.

The mean arterial pressure drop (PDmean) from AAo to the common iliac arteries during a cardiac cycle is also calculated. It is 6.29mmHg for the initial model of PI and 4.70mmHg for the final model (53months post-TEVAR), which is slightly higher than that in normal aorta for the studied segment (4mmHg[29]). The PDmean of PII at the initial and final (35months post-TEVAR) models are 6.53mmHg and 6.07mmHg, respectively, consistent with its insufficient TL remodeling.

In the final examination of PI (PI-7), V_{FL} is slightly increased, D and W_{FL} also increase at L3 (Fig.2); however, the flow exchange and tear size at this stage are both reduced. Fig.5e displays the pressure distribution at systolic peak (Psys) on a slice of FL for PI-6~7. It shows that the smaller tear size reduces the flow entering FL, however, it increases the velocity and induces higher pressure impact on the outer wall of FL (indicated by arrows in Fig.5e). The highest pressure of the impact region in PI and PII at final examination are 114.37 and 115.41mmHg respectively. Besides, by blanking the region with Psys<109.15mmHg, which is the 95% of the averaged maximum pressure in PI and PII at final examination, Fig.5f shows that the high pressure region (in red) in the FL of PII is much larger than that in PI. In fact, the FL growth rates of PI and PII at the final examination are 0.22mm^3/day and 68.61mm^3/day respectively.

Luminal Pressure Difference, Wall Shear Stress and Relative Residence Time

To investigate the pressure difference (PDiff) between TL and FL, a series of slices that are perpendicular to the centerline of TL are extracted and the net pressures in TL (P_{TL}) and FL (P_{FL}) on each slice over a cardiac cycle are calculated. Fig.6 displays PDiff (PDiff=P_{FL}-P_{TL}) in each model. In both patients, pre-TEVAR (Fig.6a,6e), P_{FL} is smaller than P_{TL} at the level above AoT-2; while, below AoT-2, P_{FL} is larger than P_{TL}, pushing the FL towards TL. Post- TEVAR, the primary entry is closed. In PI, negative values of PDiff are found above AoT-3 (Fig.6b~c), indicating higher P_{TL} presents in this region, which supports the aortic wall and assists in TL expansion. However, in the region below AoT-3 in PI, due to the blood perfusion into the FL, positive values of PDiff present, indicating FL propulsion on the TL. In the final follow-up of PI (Fig.6d), the maximum value of PDiff is 0.22mmHg. This maximum PDiff occurs close to L3. At this position, W_{FL} and W_{TL} increase by 1.02mm and 0.46mm respectively (Fig.2), indicating this small value of PDiff (0.22mmHg) is not large enough to squeeze TL but the local pressure in FL (Fig.5e) is able to induce further FL expansion. On the other hand, in PII, post-TEVAR, AoT-2 becomes the main inlet of the flow into FL. Higher above this tear, P_{TL} is larger than P_{FL}, supporting TL expansion (Fig.6e~f). In the near region above AoT-2, TL remodeling is insufficient for the short-term follow-ups but P_{FL} gradually increases; thus, regional positive PDiff is found in PII-3 above AoT-2 (arrow indicated in Fig.6f). Below AoT-2, positive values of PDiff dominate and the maximum PDiff in the final examination of PII is 1.39mmHg, more than 6-times as high as that in PI, occurring close to L3. Taking account of that, in PII-5, W_{TL} decreases yet W_{FL} increases at L3 (Fig.2d~e), this high PDiff propels TL collapse and the local pressure pushes FL growth.

Fig.7 shows the wall shear stress (WSS) distribution on the flap at systolic peak. Its variation over a cardiac cycle is shown in Video S1-6, Supporting Document. In both patients, the WSS on the flap at the FL side (WSS_{FL}) is significantly smaller than that on the TL side (WSS_{TL}); and the WSS_{TL} in PII is generally higher than that in PI. At initial presentation, the maximum WSS_{TL} occurs at the edge of primary entry; while the maximum WSS_{FL} occurs at the proximal descending aorta along the side opposite to the primary entry (indicated by arrows in Fig.7b). In follow-ups, the maximum WSS_{TL} occurs at the region where TL presents most collapse; while the maximum WSS_{FL} occurs at the edge of the tears. AoT-3 and AoT-2 are the main FL flow entries for PI and PII in follow-ups, which induces helical flow in the downstream and high WSS_{FL} on the side opposite to the tears (indicated by hollow arrows in Fig.7b). To further visualize the variation of WSS_{FL} at different regions along the flap on the FL side, the color map is assigned to 0~5Pa (Fig.7c) and 0~0.5Pa (Fig.7d) to show the distal and proximal region respectively. In PI, WSS_{FL} at the region below AoT-3 reduces obviously from PI-4 to PI-6; however, in the final examination, it is slightly increased, although the maximum WSS_{FL} in this region is still smaller than 1Pa. In PII, WSS_{FL} presents obvious increase in PII-4 and reduces slightly in PII-5; the maximum WSS_{FL} at the region between AoT-2 and AoT-3 in the final examination is 5.21Pa.

Particle residence time is proposed to be related to thrombosis establishment[14].

The relative residence time (RRT), which is based on the time-averaged WSS (TAWSS) and oscillatory shear index (OSI), $[(1\text{-}2\cdot\mathrm{OSI})\cdot\mathrm{TAWSS}]^{-1}$, reflects particle residence time and thus may correspond with the region of thrombosis[14, 30]. Fig.8a~b show the RRT distributions (normalized by the maximum RRT value) in PI and PII post-TEVAR, respectively. In PI, the highest RRT occurs at the FL proximal tip in PI-2~5; while in PI-6~7, RRT is greatly decreased and the highest RRT no longer occurs at the FL tip. In PII, the highest RRT also occurs at the FL proximal tip. Fig.8d displays the variation of the maximum RRT (normalized by the maximum RRT at the first follow-up, *i.e.* PI-2 and PII-2 for PI and PII respectively). The RRT variation in PI and PII shows significant difference during short-term follow-up: the normalized maximum RRT in PI increases greatly in PI-3 (from 1 to 5.516) and gradually decreases afterwards to 0.00405 in PI-7; while in PII, it decreases in PII-3 (from 1 to 0.025) and then maintains between 0.00324-0.319. The difference in the maximum RRT's variation pattern shows potential to predict different FL remodeling in the two patients.

DISCUSSION

Thoracic endografts, aiming to seal the primary entry and diverting blood flow into TL, are increasingly used in treating type-B aortic dissection[31]. Ideally, this approach would lead to thrombosis establishment in the FL and morphologic change in TL, to stabilize the aorta and consequently reduce aorta-related death. Previous studies confirmed the favorable results of TEVAR; however, also reported FL expansion on the segment distal to endografts, usually in the infrarenal aorta[32, 33]. This is related to the patency of FL[33] or, in other words, it is related to the flow field and hemodynamic conditions in AoD. Current literatures provide little information concerning the fate of the abdominal aorta post-TEVAR and, to our knowledge, computational studies on long-term multiple follow-up cases that are able to report the change of hemodynamic parameters have been lacking. Therefore, in the current study, we investigate two patients showing similar physical and hemodynamic features at initial presentation but presenting different FL development (stable in PI and expanded in PII) during the follow-ups. We preliminarily identify the possible hemodynamic parameters that could help to evaluate/predict FL enlargement and thrombosis formation. In this study, the variation trends of the hemodynamic parameters are more important than their absolute values.

The mechanical load acting on the FL boundary, which includes the outer wall of FL and the flap, induces FL enlargement and at the same time restricts TL remodeling. The pressure that is normally applied on the FL wall plays a key role in luminal remodeling[34] and the local flow directly relates to its distribution and magnitude. The flow can be assessed by its amount and the velocity. The first is mainly related to the size of tears. By comparing Fig.4b~c and Table 1, it can be found that the absolute flow mass passes each tear per second has positive relationship with the size of the tear. This can be shown on AoT-3 of PI and AoT-2~3 of PII, since they have multiple follow-up data, and it is consistent with previous report[14]. The second, velocity, is determined by both the flow rate as well as the tear size; a smaller tear size is correspondent to smaller flow rate yet accelerates the flow at the same time. For instance, in the final two examinations of PI (PI-6 and PI-7), the amount of the blood entering FL via AoT-3 decreases from 5.43% to 3.09% of the total flow and the tear size decreases from 93.49mm^2 to 44.09mm^2. However, the flow passing this tear has been accelerated and induces stronger impact on the FL outer wall (Fig.5e). If studying a longer period (PI-4~7), the variation of W_{FL} at L3 (Fig.2e), where just below AoT-3 in PI, is similar to the variation of the ratio between the diverted flow amount and the tear size.

Along the aorta, the pressure in TL decreases generally but that in FL, due to the vortical flow and its higher energy exchange, it does not present significant spatial difference. The AoTs, functioning as the bridge between TL and FL, transport blood flow and also pressure gradient. This induces similar pressure in the TL and FL near the tears. Because of the relatively uniform P_{FL} and its connection with P_{TL} at the tears, in general, P_{FL} is smaller than P_{TL} in the proximal region (above the AoTs) and higher than P_{TL} in the downstream. This general distribution feature is shown in Fig.5 in all of the post-interventional cases at the moment of systolic peak and similar patterns can be found in other time steps of the cardiac cycle.

At the flap, P_{FL} and P_{TL} conflict each other; the difference between them (PDiff) may be associated with subsequent luminal remodeling[14]. Luminal remodeling is a long-term effect; investigation of PDiff in short-term follow-ups may show the variation trends of lumen remodeling, while PDiff in long-term follow-ups may be consistent to lumen remodeling results. Indeed, taking L3 as an example, in short-term (PI-2~3, PII-2~3), PD in PII increases from 1.44 to 2.93mmHg (7days-1month);

while, PDiff in PI remains about 0.55mmHg (7days-4month). This, earlier than luminal change (Fig.2), shows the potential of FL enlargement for PII. In long-term follow-ups (PI-4~7, PII-4~5), AoT-3 becomes the main FL flow entry in PI and AoT-2 is the main entry in PII. PDiff increases from negative to positive slightly below the position of AoT-3 in PI and AoT-2 in PII. Moreover, in both patients, in the final examination, the maximum PDiff occurs near L3, where W_{FL} increases the most (among the compared four positions) and W_{TL} in PII decreases. The abovementioned indicates: (i) in short-term follow-ups, great increase of PDiff may imply potential FL expansion; (ii) while, in long-term follow-up, the position of the first flow entry of FL is the negative-to-positive watershed of PDiff, the position of the maximum PDiff is consistent with the greatest W_{FL} increase, and when the maximum PDiff is small (0.22mmHg in PI-7), the pressure induces slight FL expansion without restricted acts on TL, but when it is relatively large (1.39mmHg in PII-5), both FL expansion and TL collapse are found. In clinical examinations, monitoring PDiff at early-stage and identifying the position of FL entries and the position of largest PDiff may assist in wisely control of the untreated aorta segment.

The WSS is related to the formation of thrombosis. Previous studies suggested that the tearing of the aortic wall and high WSS in the near region of the tears could promote initial activation of platelets as well as the formation of platelet aggregates; while, the highly vortical flow pattern in the FL corresponding with low WSS promotes platelet aggregation and deposition, so that leads to surface thrombosis [35, 36]. In other words, lower WSS may induce surface thrombus and thus lead to constructive FL remodeling [37, 38]. In the long-term follow-ups (PI-4~5 and PII-4~5), complete thrombosis is found at the proximal region of dissection and partial thrombosis remains above the re-entries. The partial thrombosis in both PI and PII is aligned with the intimal flap; thus, WSS on the flap along the TL and FL sides are compared. The WSS_{FL} is significantly lower than WSS_{TL} throughout the cardiac cycle; the low WSS_{FL} possibly induces surface thrombus along the flap in FL while the high WSS_{TL} can keep the TL patent. The lowest WSS_{FL} (<0.25Pa) occurs at the proximal region of FL (Fig.7d), implying potential thrombosis in these regions. Indeed, partial thrombosis in PI-4~5 with very low WSS_{FL} turns to complete thrombosis in PI-6~7 (indicated by arrow inFig.7d). Moreover, in PII, the WSS_{FL} at the tip of the flap in PII-3 is small (<0.25Pa). In its next follow-up (PII-4), growth of partial thrombosis can be found (indicated by arrow in Fig.7d). However, slightly higher WSS_{FL} is shown in PII-4 at the proximal tip, and in its next follow-up (PII-5), the partial thrombosis is slightly reduced (indicated by hollow arrow in Fig.7d). This indicates the surface thrombosis is possibly very sensitive to WSS, and during the long-term recovery, FL regression/growth could be repeatedly occurred at the proximal tip of the FL.

The derived parameter of shear stress - RRT is related to particle residence and may reflect thrombosis establishment as well[14]. To identify the location of high RRT, Fig.8a~b draw the distribution of the normalized RRT to its maximum value in each model. It shows that high RRT corresponds to the region with highly vortical and low velocity flow. This occurs at the FL proximal tip for both the patients (PI-2~5, PII-2~5). Moreover, Fig.8ccompares the magnitude of RRT in PI-5 and PII-4, in which the follow-up periods are similar (21 and 18months for PI and PII respectively). The maximum RRT in PI-5 and PII-4 are 68.94 and 70.66Pa^{-1} respectively. The similar distribution pattern and magnitude of RRT in PI and PII indicates that the values of RRT alone may not be able to predict FL remodeling. To further investigate this, the variation of the maximum RRT is studied (Fig.8d). The maximum RRTs in PI-3~7 and PII-3~5 are normalized to the correspondent first follow-up results (PI-2 and PII-2, 7days post-TEVAR). The variation patterns of this normalized maximum RRT show significant difference between PI and PII. This implicates that, post-TEVAR, variation of RRT in short- to middle-term follow-up (PI-2~5, PII-2~4) may play a key role in thrombosis establishment: an increase of RRT after TEVAR and maintaining the relative normalized maximum RRT value to be above 1.0 (Fig.8d) may lead to positive FL remodeling.

Common morphological predictors for re-intervention or surgery after TEVAR include aortic diameter >55mm and growth rate >10mm/year [39]. Hemodynamic condition of the dissected aorta plays an important role in driving TL and FL remodeling. In other words, hemodynamic parameters may have the potential to predict the dissection development earlier than morphological change. However, hemodynamic markers that can possibly predict FL development post-TEVAR have not been proposed yet, which would require long-term multiple follow-up analyses. The current study investigated the correlation of hemodynamic parameters to the development of post-TEVAR dissection. It preliminarily proposed the parameters that are potential to differentiate the enlarged and stable FL in an early stage post-TEVAR. Although this study was based on a limited number of patient cases and thus no clinical conclusion can be drawn at this stage, it is the basis to future studies on a larger amount of patient cases and would contribute to the research regarding early decision-making on re-intervention or surgery for AoD after TEVAR.

LIMITATIONS

This study, based on long-term multiple follow-up data of two patients, preliminarily shows the relationship of the variations between hemodynamic parameters and luminal remodeling. However, critical values of these parameters should be better determined by involving a greater number of patient cases. Besides, more detailed mechanical analysis should involve the fluid-structure interaction analysis, which does not only provide the stress information in the aortic wall but also offer more accurate results on the WSS. However, due to the complex geometry and the lack of the actual material properties, the existed fluid-structure interaction studies on AoD often generate the aortic/dissection wall with arbitrary thickness and assume the mechanical properties of the aortic and dissection wall similar to the properties of aortic aneurysms. More accurate simulations are highly dependent on accurate model establishment and material property measurements, which are currently carried on in our laboratory.

ACKNOWLEDGEMENTS

This study was supported by National Natural Science Foundation of China (81471752, 81353265), National Science and Technology Pillar Program of China (2015BAI04B03), and National Key Research and Development Program of China (2017YFC0107900). PW was partially supported by UK EPSRC (EP/N014642/1).

CONFLICTS OF INTEREST

No

ETHICAL APPROVAL

This study was approved by the Institutional Review Board of Chinese PLA General Hospital (ref no. 20110903.V1.1)

REFERENCES

1. Younes, H.K., P.W. Harris, J. Bismuth, K. Charlton-Ouw, E.K. Peden, A.B. Lumsden, and M.G. Davies, Thoracic endovascular aortic repair for type B aortic dissection. Ann Vasc Surg 2010; 24: p. 39-43.
2. Weber, T.F., D. Bockler, M. Muller-Eschner, M. Bischoff, M. Kronlage, H. von Tengg-Kobligk, H.U. Kauczor, and A. Hyhlik-Durr, Frequency of abdominal aortic expansion after thoracic endovascular repair of type B aortic dissection. Vascular 2016; 24: p. 567-79.
3. Doyle, B.J. and P.E. Norman, Computational Biomechanics in Thoracic Aortic Dissection: Today's Approaches and Tomorrow's Opportunities. Ann Biomed Eng 2016; 44: p. 71-83.
4. Saad, A.A., T. Loupas, and L.G. Shapiro, Computer vision approach for ultrasound Doppler angle estimation. J Digit Imaging 2009; 22: p. 681-88.
5. Muller-Eschner, M., F. Rengier, S. Partovi, R. Unterhinninghofen, D. Bockler, S. Ley, and H. von Tengg-Kobligk, Tridirectional phase-contrast magnetic resonance velocity mapping depicts severe hemodynamic alterations in a patient with aortic dissection type Stanford B. J Vasc Surg 2011; 54: p. 559-62.
6. Stadlbauer, A., W. van der Riet, S. Globits, G. Crelier, and E. Salomonowitz, Accelerated phase-contrast MR imaging: comparison of k-t BLAST with SENSE and Doppler ultrasound for velocity and flow measurements in the aorta. J Magn Reson Imaging 2009; 29: p. 817-24.
7. Kohler, B., U. Preim, M. Grothoff, M. Gutberlet, K. Fischbach, and B. Preim, Motion-aware stroke volume quantification in 4D PC-MRI data of the human aorta. Int J Comput Assist Radiol Surg 2016; 11: p. 169-79.
8. Sakalihasan, N., C.A. Nienaber, R. Hustinx, P. Lovinfosse, M. El Hachemi, J.P. Cheramy-Bien, L. Seidel, J.P. Lavigne, J. Quaniers, M.A. Kerstenne, A. Courtois, A. Ooms, A. Albert, J.O. Defraigne, and J.B. Michel, (Tissue PET) Vascular metabolic imaging and peripheral plasma biomarkers in the evolution of chronic aortic dissections. Eur Heart J Cardiovasc Imaging 2015; 16: p. 626-33.
9. Nchimi, A., J.P. Cheramy-Bien, T.C. Gasser, G. Namur, P. Gomez, L. Seidel, A. Albert, J.O. Defraigne, N. Labropoulos, and N. Sakalihasan, Multifactorial relationship between 18F-fluoro-deoxy-glucose positron emission tomography signaling and biomechanical properties in unruptured aortic aneurysms. Circ Cardiovasc Imaging 2014; 7: p. 82-91.
10. Alimohammadi, M., O. Agu, S. Balabani, and V. Diaz-Zuccarini, Development of a patient-specific simulation tool to analyse aortic dissections: assessment of mixed patient-specific flow and pressure boundary conditions. Med Eng Phys 2014; 36: p. 275-84.
11. Karmonik, C., M. Muller-Eschner, S. Partovi, P. Geisbusch, M.K. Ganten, J. Bismuth, M.G. Davies, D. Bockler, M. Loebe, A.B. Lumsden, and H. von Tengg-Kobligk, Computational fluid dynamics investigation of chronic aortic dissection hemodynamics versus normal aorta. Vasc Endovascular Surg 2013; 47: p. 625-31.
12. Shang, E.K., D.P. Nathan, R.M. Fairman, J.E. Bavaria, R.C. Gorman, J.H. Gorman, 3rd, and B.M. Jackson, Use of computational fluid dynamics studies in predicting aneurysmal degeneration of acute type B aortic dissections. J Vasc Surg 2015; 62: p. 279-84.
13. Tse, K.M., P. Chiu, H.P. Lee, and P. Ho, Investigation of hemodynamics in the development of dissecting aneurysm within patient-specific dissecting aneurismal aortas using computational fluid dynamics (CFD) simulations. J Biomech 2011; 44: p. 827-36.
14. Cheng, Z., N.B. Wood, R.G. Gibbs, and X.Y. Xu, Geometric and flow features of type B aortic dissection: initial findings and comparison of medically treated and stented cases. Ann Biomed Eng 2015; 43: p. 177-89.
15. Chen, D., M. Muller-Eschner, H. von Tengg-Kobligk, D. Barber, D. Bockler, R. Hose, and Y. Ventikos, A patient-specific study of type-B aortic dissection: evaluation of true-false lumen blood exchange. Biomed Eng Online 2013; 12: p. 65.
16. Karmonik, C., J. Bismuth, M.G. Davies, D.J. Shah, H.K. Younes, and A.B. Lumsden, A computational fluid dynamics study pre- and post-stent graft placement in an acute type B aortic dissection. Vasc Endovascular Surg 2011; 45: p. 157-64.
17. Cheng, S.W., E.S. Lam, G.S. Fung, P. Ho, A.C. Ting, and K.W. Chow, A computational fluid dynamic study of stent graft remodeling after endovascular repair of thoracic aortic dissections. J Vasc Surg 2008; 48: p. 303-9.
18. Chen, D., M. Muller-Eschner, D. Kotelis, D. Bockler, Y. Ventikos, and H. von Tengg-Kobligk,

A longitudinal study of Type-B aortic dissection and endovascular repair scenarios: computational analyses. Med Eng Phys 2013; 35: p. 1321-30.

19. Karmonik, C., J. Bismuth, D.J. Shah, M.G. Davies, D. Purdy, and A.B. Lumsden, Computational study of haemodynamic effects of entry- and exit-tear coverage in a DeBakey type III aortic dissection: technical report. Eur J Vasc Endovasc Surg 2011; 42: p. 172-7.
20. Naim, W.N.W.A., P. Ganesan, Z. Sun, K. Osman, and E. Lim, The impact of the number of tears in patient-specific stanford type B aortic dissecting aneurysm: CFD simulations. J Mech Med Biol 2014; 14: p. 1450017.
21. Alimohammadi, M., J.M. Sherwood, M. Karimpour, O. Agu, S. Balabani, and V. Diaz-Zuccarini, Aortic dissection simulation models for clinical support: fluid-structure interaction vs. rigid wall models. Biomed Eng Online 2015; 14: p. 34.
22. Qiao, A., W. Yin, and B. Chu, Numerical simulation of fluid-structure interaction in bypassed DeBakey III aortic dissection. Comput Methods Biomech Biomed Engin 2015; 18: p. 1173-80.
23. Clough, R.E., V.E. Zymvragoudakis, L. Biasi, and P.R. Taylor, Usefulness of new imaging methods for assessment of type B aortic dissection. Ann Cardiothorac Surg 2014; 3: p. 314-8.
24. Birjiniuk, J., J.M. Ruddy, E. Iffrig, T.S. Henry, B.G. Leshnower, J.N. Oshinski, D.N. Ku, and R.K. Veeraswamy, Development and testing of a silicone in vitro model of descending aortic dissection. J Surg Res 2015; 198: p. 502-7.
25. Soudah, E., P. Rudenick, M. Bordone, B. Bijnens, D. Garcia-Dorado, A. Evangelista, and E. Onate, Validation of numerical flow simulations against in vitro phantom measurements in different type B aortic dissection scenarios. Comput Methods Biomech Biomed Engin 2015; 18: p. 805-15.
26. Vignon-Clementel, I.E., C.A. Figueroa, K.E. Jansen, and C.A. Taylor, Outflow boundary conditions for three-dimensional finite element modeling of blood flow and pressure in arteries. Comput Methods Biomech Biomed Engin 2006; 195: p. 3776-96.
27. Ganten, M.K., T.F. Weber, H. von Tengg-Kobligk, D. Bockler, W. Stiller, P. Geisbusch, G.W. Kauffmann, S. Delorme, M. Bock, and H.U. Kauczor, Motion characterization of aortic wall and intimal flap by ECG-gated CT in patients with chronic B-dissection. Eur J Radiol 2009; 72: p. 146-53.
28. Papaharilaou, Y., D.J. Doorly, and S.J. Sherwin, The influence of out-of-plane geometry on pulsatile flow within a distal end-to-side anastomosis. J Biomech 2002; 35: p. 1225-39.
29. Bortolotto, L.A. and M.E. Safar, Blood pressure profile along the arterial tree and genetics of hypertension. Arq Bras Cardiol 2006; 86: p. 166-9.
30. Gorring, N., L. Kark, A. Simmons, and T. Barber, Determining possible thrombus sites in an extracorporeal device, using computational fluid dynamics-derived relative residence time. Comput Methods Biomech Biomed Engin 2015; 18: p. 628-34.
31. Nienaber, C.A., S. Kische, H. Ince, and R. Fattori, Thoracic endovascular aneurysm repair for complicated type B aortic dissection. J Vasc Surg 2011; 54: p. 1529-1533.
32. Andacheh, I.D., C. Donayre, F. Othman, I. Walot, G. Kopchok, and R. White, Patient outcomes and thoracic aortic volume and morphologic changes following thoracic endovascular aortic repair in patients with complicated chronic type B aortic dissection. J Vasc Surg 2012; 56: p. 644-50.
33. Sigman, M.M., O.P. Palmer, S.W. Ham, M. Cunningham, and F.A. Weaver, Aortic morphologic findings after thoracic endovascular aortic repair for type B aortic dissection. JAMA Surg 2014; 149: p. 977-83.
34. Sueyoshi, E., I. Sakamoto, K. Hayashi, T. Yamaguchi, and T. Imada, Growth rate of aortic diameter in patients with type B aortic dissection during the chronic phase. Circulation 2004; 110: p. II256-61.
35. Sheriff, J., D. Bluestein, G. Girdhar, and J. Jesty, High-shear stress sensitizes platelets to subsequent low-shear conditions. Ann Biomed Eng 2010; 38: p. 1442-50.
36. Goel, M.S. and S.L. Diamond, Adhesion of normal erythrocytes at depressed venous shear rates to activated neutrophils, activated platelets, and fibrin polymerized from plasma. Blood 2002; 100: p. 3797-803.
37. Wu, M.H., Y. Kouchi, Y. Onuki, Q. Shi, H. Yoshida, S. Kaplan, R.F. Viggers, R. Ghali, and L.R. Sauvage, Effect of differential shear stress on platelet aggregation, surface thrombosis, and endothelialization of bilateral carotid-femoral grafts in the dog. J Vasc Surg 1995; 22: p. 382-90.

38. Menichini, C., Z. Cheng, R.G. Gibbs, and X.Y. Xu, Predicting false lumen thrombosis in patient-specific models of aortic dissection. J R Soc Interface 2016; 13: p. 20160759.
39. Erbel, R., V. Aboyans, C. Boileau, E. Bossone, R.D. Bartolomeo, H. Eggebrecht, A. Evangelista, V. Falk, H. Frank, O. Gaemperli, M. Grabenwoger, A. Haverich, B. Iung, A.J. Manolis, F. Meijboom, C.A. Nienaber, M. Roffi, H. Rousseau, U. Sechtem, P.A. Sirnes, R.S. Allmen, and C.J. Vrints, 2014 ESC Guidelines on the diagnosis and treatment of aortic diseases: Document covering acute and chronic aortic diseases of the thoracic and abdominal aorta of the adult. The Task Force for the Diagnosis and Treatment of Aortic Diseases of the European Society of Cardiology (ESC). Eur Heart J 2014; 35: p. 2873-926.

FIGURE LEGENDS

Fig.1 (a)~(d) display the reconstructed models of AoD (D-days, M-months); (e) is a sonogram of Doppler ultrasound velocimetry, the upper edge of which is shown in green; (f) shows an axial slice of CTA scan at initial presentation of PI, in which the segmented lumen boundary is shown in yellow.

Fig.2 The luminal remodeling. (a) displays the measured axial positions (L1-4) and the regions to calculate luminal volume (V_{TL}, V_{TL} -Part and V_{FL}); (b)~(e) show the variation of luminal volume, aortic diameter, width of TL and FL respectively.

Fig.3 Flow patterns of AoD. (a)~(b) display the flow streamlines at systolic peak; (c) shows the streamlines at the proximal region of FL in the final model of PII.

Fig.4 Flow exchange between the true and false lumen. (a) displays the variation of the mass flow rate towards the FL via the primary entry, AoT-2 and AoT-3 over a cardiac cycle at initial presentation; (b) and(c) respectively show the mass flow rate variation at AoT-2 and AoT-3 during the longitudinal follow-ups.

Fig.5 Pressure distribution along the dissected aorta. (a) and (b) display the PDsys distribution in PI and PII respectively; (c) shows the PDsys in a normal aorta; (d) displays the variation of the maximum PDsys during the follow-up; (e) shows the Psys at a slice crossing the FL in the final two examinations of PI and in the final examination of PII; and (f) shows the region with Psys$\geqslant$ 09.15mmHg (in red).

Fig.6 Pressure difference between FL and TL for PI (a)~(d) and PII (e)~(f).

Fig.7 WSS distribution along the flap. (a) and (b) display the WSS distribution at systolic peak on the flap of TL and FL side respectively; (c) and (d) show the WSS distribution on the flap of FL side during the long-term follow-ups in different WSS ranges.

Fig.8 RRT distribution and variation. (a) and (b) show the normalized RRT to its maximum value post-TEVAR in PI and PII respectively; (c) shows the RRT distribution at PI-5 and PII-4, where the follow-up periods in PI and PII are similar; and (d) displays the variation of the normalized maximum RRT to its value in the first follow-up (PI-2 for PI and PII-2 for PII).

Figure 1

FIGURE 1

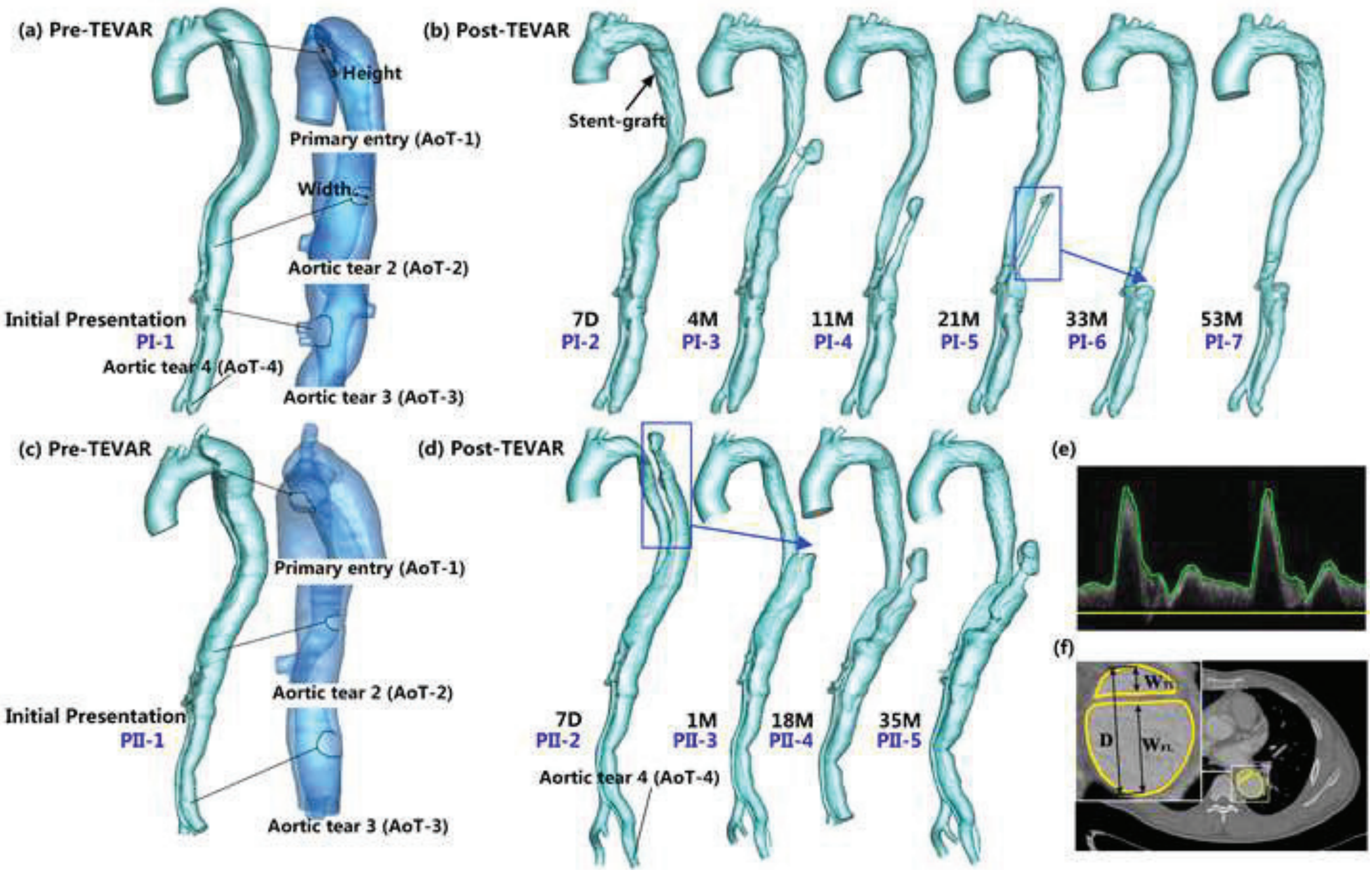

Figure 2

FIGURE 2

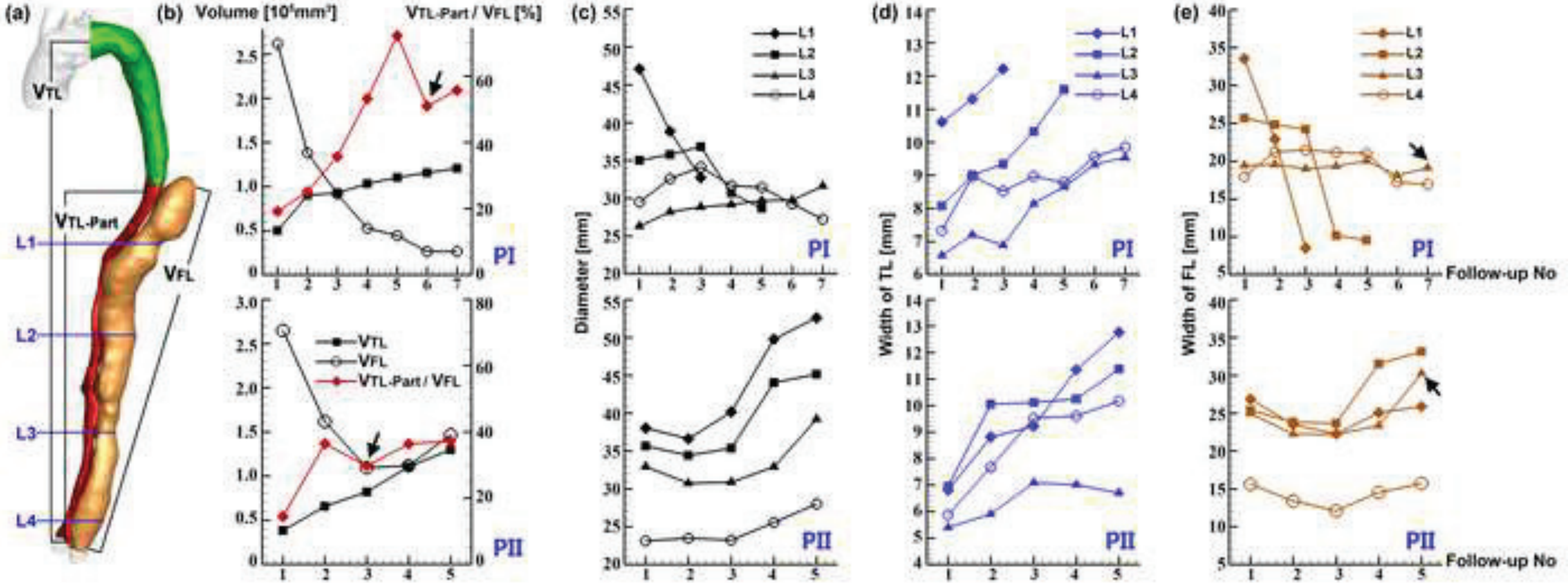

FIGURE 3

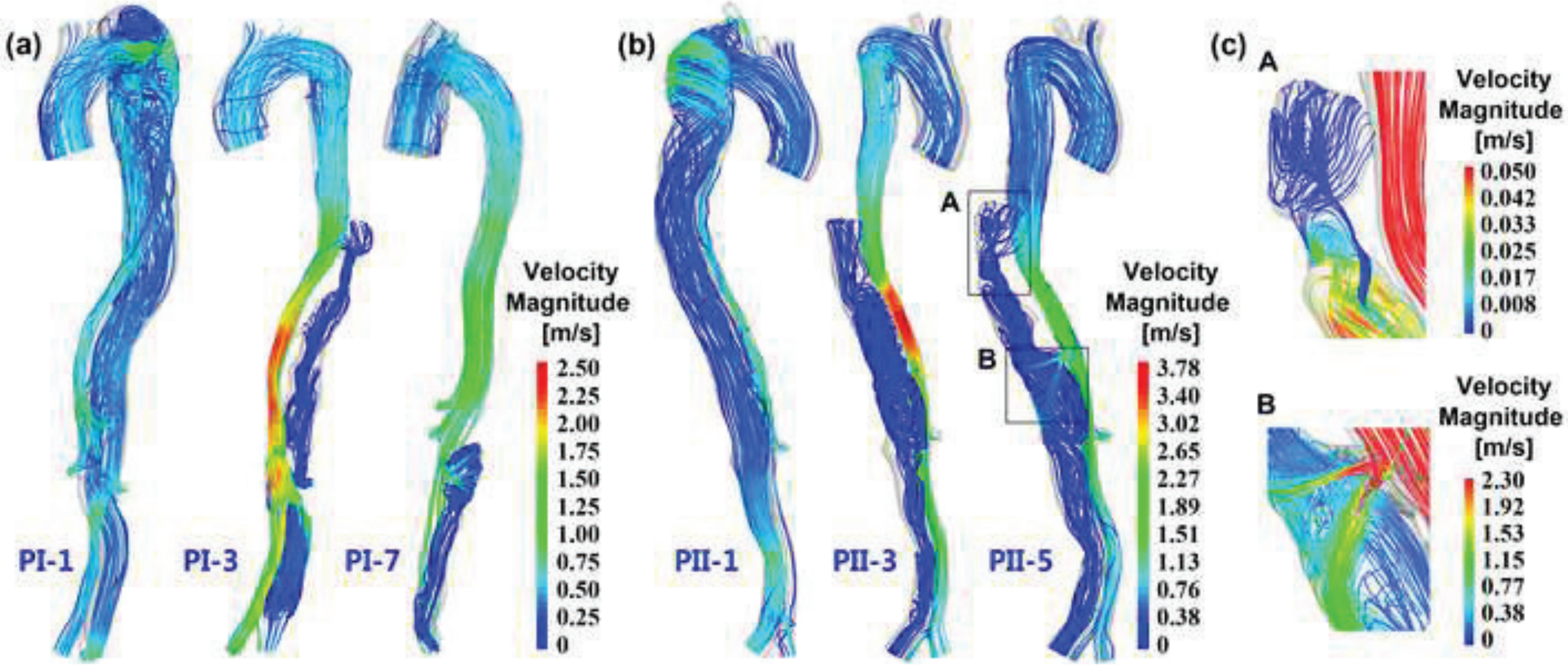
(a)
PI-1
PI-3
PI-7
Velocity
Magnitude
[m/s]
2.50
2.25
2.00
1.75
1.50
1.25
1.00
0.75
0.50
0.25
0
(b)
PII-1
PII-3
PII-5
A
B
Velocity
Magnitude
[m/s]
3.78
3.40
3.02
2.65
2.27
1.89
1.51
1.13
0.76
0.38
0
(c)
A
Velocity
Magnitude
[m/s]
0.050
0.042
0.033
0.025
0.017
0.008
0
B
Velocity
Magnitude
[m/s]
2.30
1.92
1.53
1.15
0.77
0.38
0

Figure 4

FIGURE 4

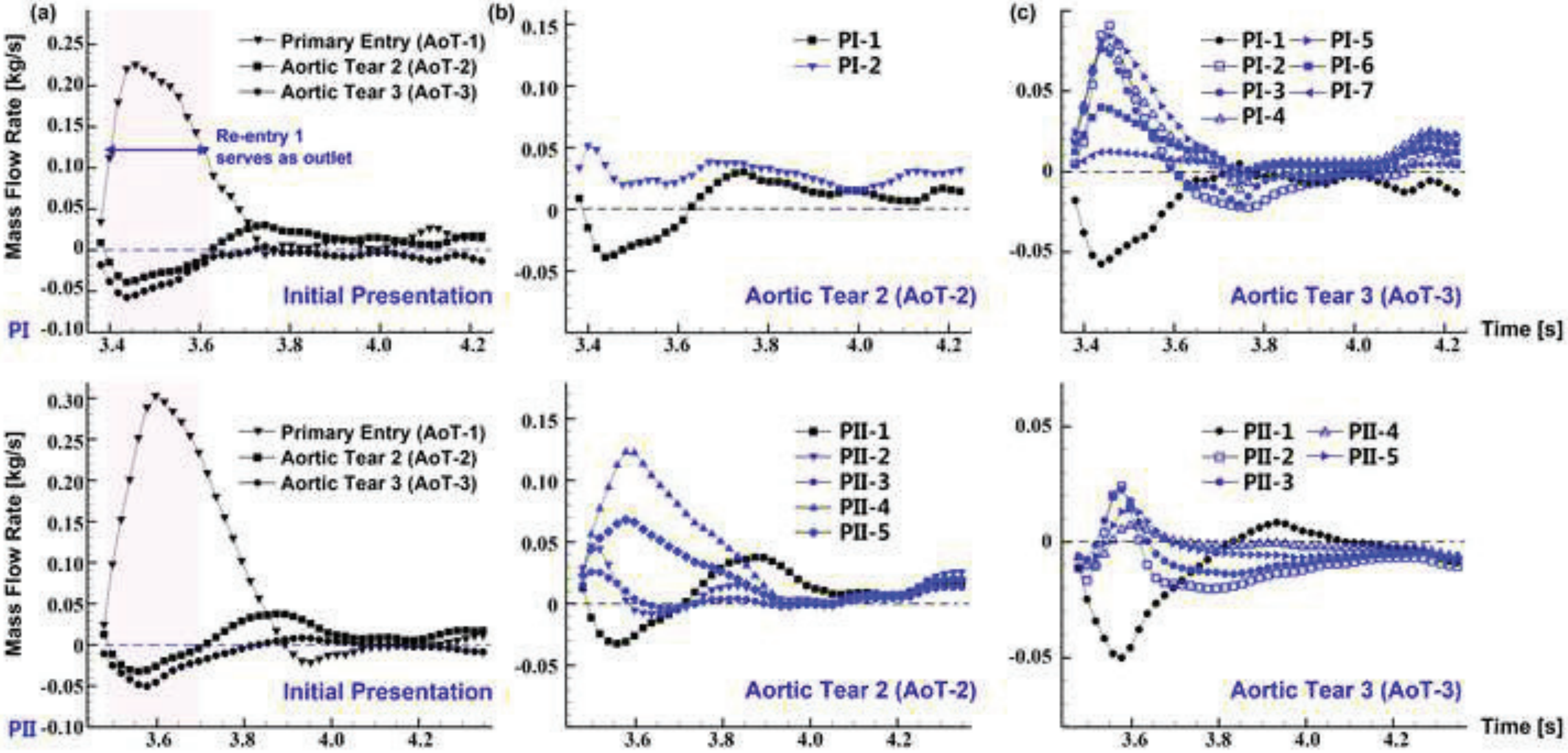

FIGURE 5

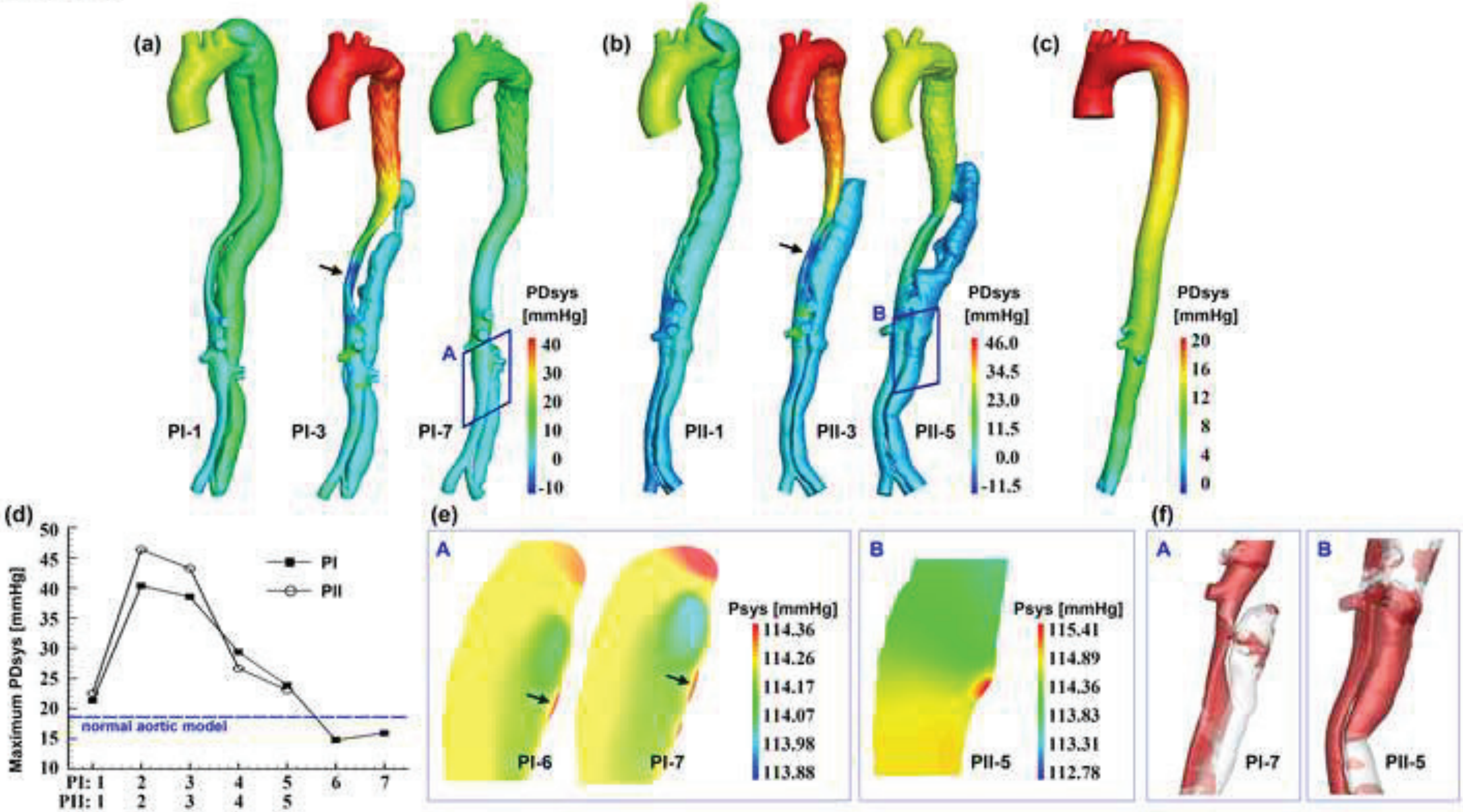
(a)
PI-1
PI-3
PI-7
A
PDsys [mmHg]
40
30
20
10
0
-10
(b)
PII-1
PII-3
PII-5
B
PDsys [mmHg]
46.0
34.5
23.0
11.5
0.0
-11.5
(c)
PDsys [mmHg]
20
16
12
8
4
0
(d)
Maximum PDsys [mmHg]
50
45
40
35
30
25
20
15
10
PI
PII
normal aortic model
PI: 1 2 3 4 5 6 7
PII: 1 2 3 4 5
(e)
A
PI-6
PI-7
Psys [mmHg]
114.36
114.26
114.17
114.07
113.98
113.88
B
PII-5
Psys [mmHg]
115.41
114.89
114.36
113.83
113.31
112.78
(f)
A
PI-7
B
PII-5

FIGURE 6

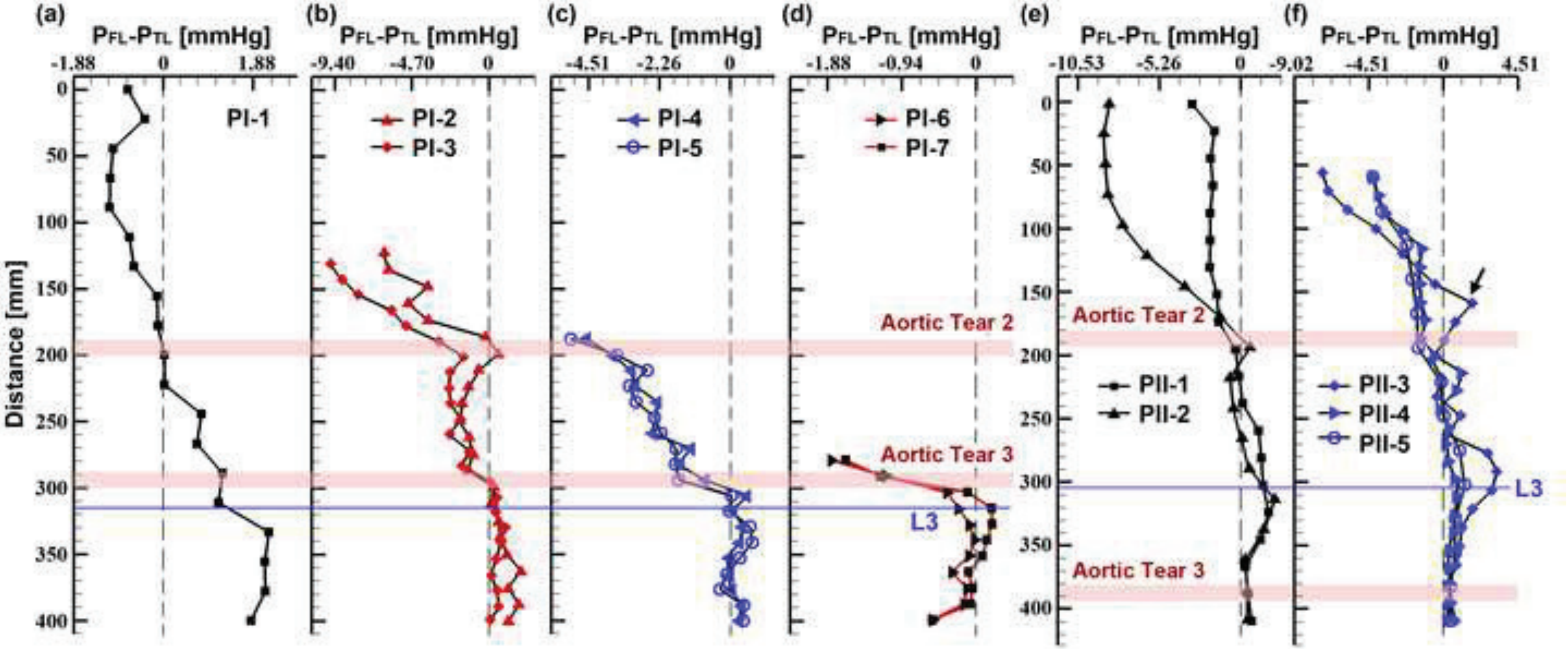
(a)
PFL-PTL [mmHg]
-1.88
0
1.88
PI-1
Distance [mm]
0
50
100
150
200
250
300
350
400
(b)
PFL-PTL [mmHg]
-9.40
-4.70
0
PI-2
PI-3
(c)
PFL-PTL [mmHg]
-4.51
-2.26
0
PI-4
PI-5
(d)
PFL-PTL [mmHg]
-1.88
-0.94
0
PI-6
PI-7
Aortic Tear 2
Aortic Tear 3
L3
(e)
PFL-PTL [mmHg]
-10.53
-5.26
0
PII-1
PII-2
Aortic Tear 2
Aortic Tear 3
(f)
PFL-PTL [mmHg]
-9.02
-4.51
0
4.51
PII-3
PII-4
PII-5
L3

Figure 7

FIGURE 7

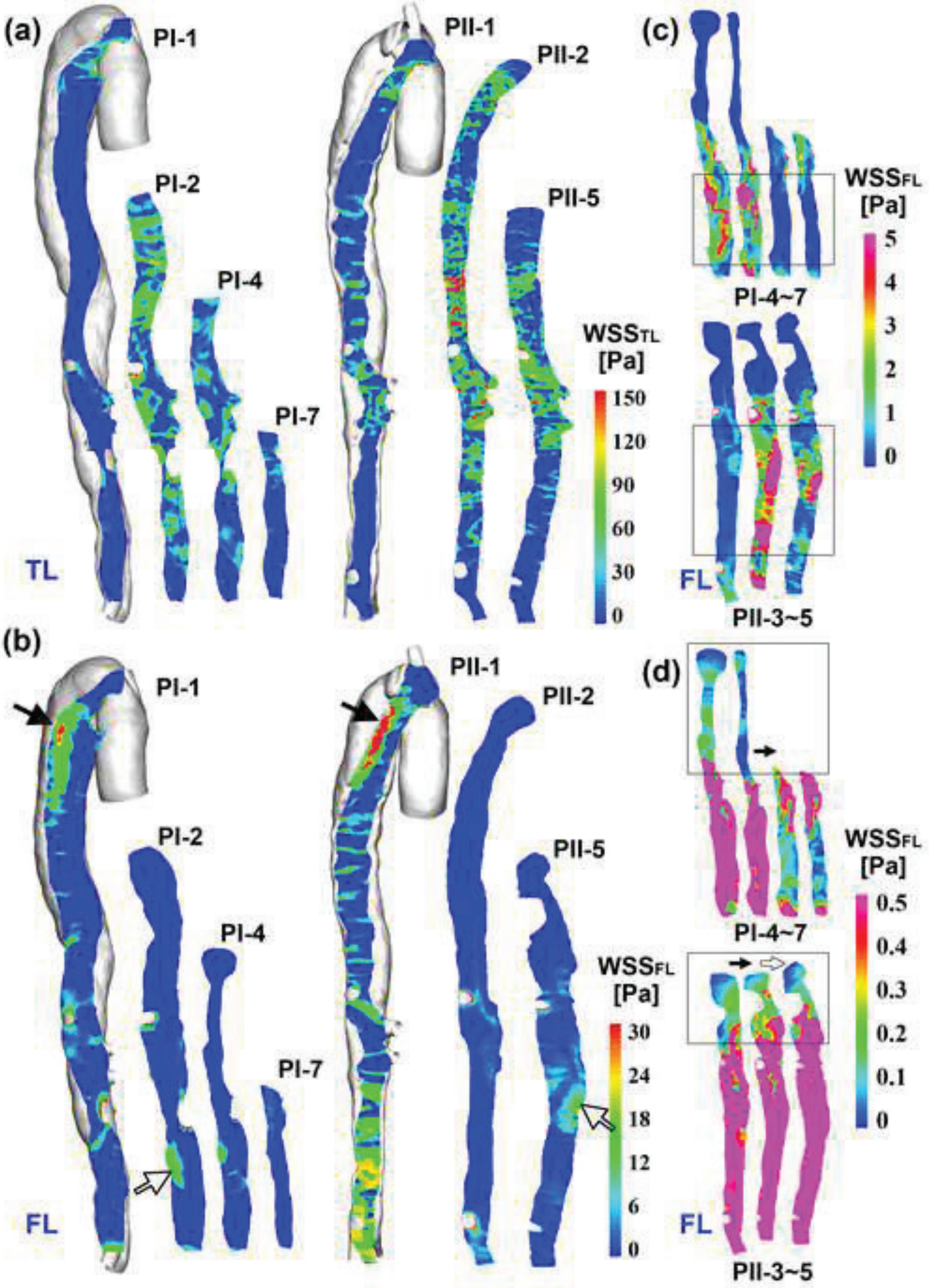

Figure 8

FIGURE 8

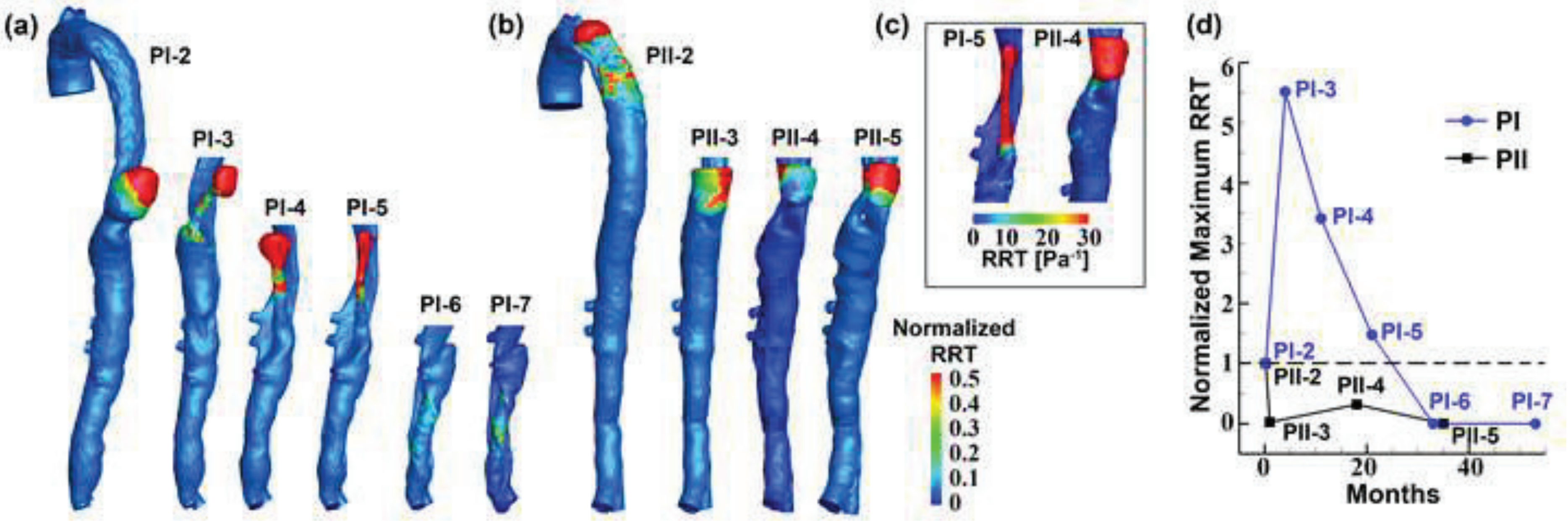

Supplementary Video 1

Supplementary Video 2

Supplementary Video 3

Supplementary Video 4

Supplementary Video 5

Supplementary Video 6